Journal of South American Earth Sciences 43 (2013) 46–61

Contents lists available at SciVerse ScienceDirect

Journal of South American Earth Sciences

journal homepage: www.elsevier.com/locate/jsames

Mineralogical and geochemical characterization of a rare ultramafic lamprophyre in the Tandilia belt basement, Río de la Plata Craton, Argentina

Jorge A. Dristas [a,*], Juan Cruz Martínez [b], Hans-Joachim Massonne [c], Marcio M. Pimentel [d]

[a] INGEOSUR and Departamento de Geología, Universidad Nacional del Sur, San Juan 670, Bahía Blanca 8000, Argentina
[b] CONICET-INGEOSUR and Departamento de Geología, Universidad Nacional del Sur, San Juan 670, Bahía Blanca 8000, Argentina
[c] Institut für Mineralogie und Kristallchemie, Universität Stuttgart, Azenbergstrasse 18, D-70174, Germany
[d] Instituto de Geociências, Campus do Vale, Universidade Federal do Rio Grande do Sul, Porto Alegre, RS 91509, Brazil

ARTICLE INFO

Article history:
Received 30 August 2012
Accepted 8 January 2013

Keywords:
Río de la Plata Craton
Ultramafic lamprophyre
Magma source
Calc-alkaline suite
Metasomatism

ABSTRACT

A metre-thick ultramafic lamprophyre dyke intrudes the basement of the Tandilia belt at the Sierra Alta de Vela, Argentina. A petrological and geochemical study of this rock and associated small dykes indicates a predominantly calc-alkaline trend. Phlogopite K–Ar dating of the ultramafic lamprophyre gave a minimum age of 1928 ± 54 Ma as a late event of the Transamazonian Orogeny, which is well represented in the basement of the Tandilia belt.

An electron microprobe study indicates the presence of phlogopite, albite, chromite and Cr-rich phenocrysts and Cr-free microphenocrysts of diopside as primary minerals. Subsequent to deformation at the contacts with the wall rock, metasomatism generated strongly zoned amphibole (edenite, pargasite, Mg-hastingite and tremolite compositions) and andradite as well as chlorite, sericite, albite, apatite and calcite. The central zone of the lamprophyre is almost undeformed and exhibits some ocellar texture. Geochemical and isotopic signatures of the lamprophyre suggest that its magma source may have previously undergone incompatible element enrichment of the mantle source, representing the original precursor magma for the calc-alkaline dyke series of the Sierra Alta de Vela.

1. Introduction

Early Proterozoic calc-alkaline and Middle Proterozoic tholeiitic dyke swarms which intrude the Rio de la Plata Craton (RLPC) in the Tandilia belt (Fig. 1) have been studied by Iacumin et al. (2001) and Teixeira et al. (2002). According to these authors the calc-alkaline dykes have andesitic to rhyolitic compositions and are of Early Proterozoic age (2.0 Ga.). The tholeiitic dyke swarms are basalts of Middle Proterozoic age (1.6 Ga) with low TiO_2 (0.9–1.7 wt. %) and high TiO_2 (up to 3.7 wt. %) contents. Associated with these suites of dykes in the Sierra Alta de Vela (SAV, south-east from the town of Tandil, Fig. 1), we have found an ultramafic lamprophyre (UML) dyke which can be related in space, time and composition to the Early Proterozoic calc-alkaline group. Additionally, hypabyssal rocks mostly from the calc-alkaline group in the form of small dykes in the SAV area were studied.

The specific aims of the current research were: 1) to determine the mineralogical and geochemical composition of the UML from the SAV, 2) to characterize the UML's magma source in order to gain new insights into the evolution of the basic dyke swarms of the Tandilia belt, 3) to describe the changes, if any, occurring in the magmas before and after crystallization, and 4) to ascertain the radiometric age of the SAV UML dyke.

2. Geological setting

The Tandilia belt in the central part of Buenos Aires province is a northwest- to southeast-trending 350 km-long and up to 60 km-wide area (Fig. 1) of outcrops in the RLPC. The basement of this belt consists of igneous-metamorphic rocks dominated by granitic to tonalitic gneisses, migmatites, and granitoids with scarce schists, marbles, amphibolites and pyroxene-rich ultramafic rocks, all part of the Buenos Aires Complex (BAC, Di Paola and Marchese, 1974). During the last decade dating by means of $^{87}Sr/^{86}Sr$ errorchrons on bulk-rock and conventional U/Pb methods and SHRIMP on zircon (Hartmann et al., 2002; Pankhurst et al., 2003; Cingolani et al.,

* Corresponding author.
E-mail address: jdristas@criba.edu.ar (J.A. Dristas).

0895-9811/$ – see front matter © 2013 Elsevier Ltd. All rights reserved.
http://dx.doi.org/10.1016/j.jsames.2013.01.002

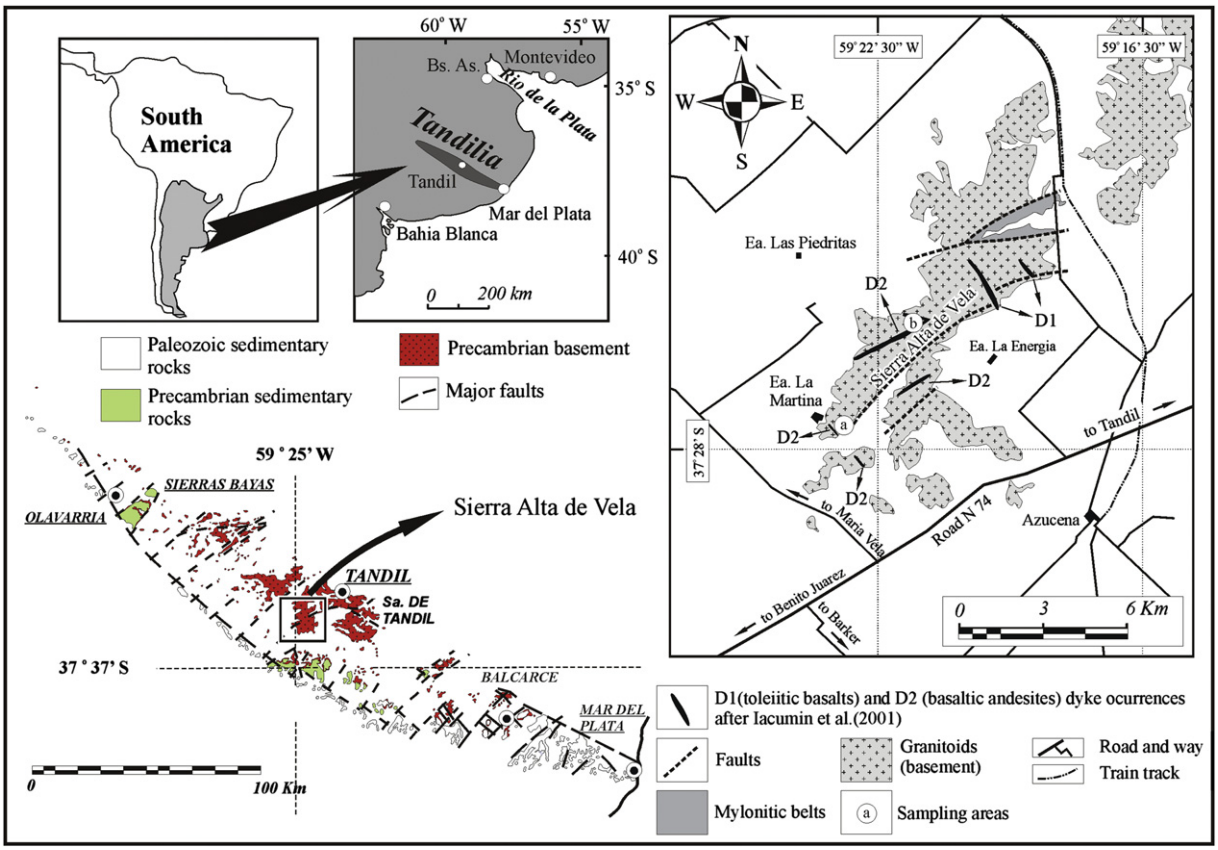

Fig. 1. Location map and geologic sketch of the Sierra Alta de Vela area, Tandilia belt (modified from Teixeira et al. (2002). Sampling area "a" involves the UML (samples 0116, 0216, 0316, SA-02) and samples 0117, 0817, 0816. Sampling area "b" corresponds to sample 0217. For chemical analyses see Table 5.

2005; Rapela et al., 2007) constrained the occurrence of igneous and metamorphic events of the BAC to the Transamazonian Orogeny (2.2–1.9 Ga), a well-known period affecting basement rocks from Uruguay and south-eastern Brazil. Iacumin et al. (2001) and Teixeira et al. (2002) characterized the Middle Proterozoic (2.0 Ga) calc-alkaline (D3 and D4) and the Early Proterozoic (1.6 Ga) tholeiitic (D1–D2) dyke swarms that intruded the Tandilia belt. These authors showed that the dyke swarms originated in depleted-to-enriched incompatible element mantle sources, and that their emplacement occurred during the transtensional to post-collisional stages of the Transamazonian Orogeny. According to Iacumin et al. (2001) and Teixeira et al. (2002), only the youngest and tholeiitic series of dykes is present in the SAV. However, Lema and Cucchi (1981, 1985) mentioned that the deformed granitic rocks (s.s.) of the SAV were cross-cut by acid dykes, which were also affected by the deformation. In addition, Dristas (1983) recognized a deformed rhyolite dyke in the basement of the Sierra del Tigre, 3 km SW of the town of Tandil. An early description of lamprophyres in the Tandilia belt was discredited by Quartino and Villar Fabre (1967), who suggested that these rocks were deformed amphibolites.

Dalla Salda and Francese (1985) reported a deformed biotitic granite east of the SAV, where the UML studied here was emplaced. Mylonitic deformation with different orientations and variable intensity has been determined in SAV granitic rocks, mainly in NNE–SSW and NE–SW direction (Lema and Cucchi, 1985; Iacumin et al., 2001).

The western and southwestern rocks of the BAC are unconformably overlain by subhorizontal Neoproterozoic to Early Palaeozoic shallow marine siliciclastic and carbonatic sedimentary rocks (Dalla Salda and Iñiguez Rodríguez, 1979; Iñiguez et al., 1989). This sedimentary succession is called the La Tinta Formation (Leveratto and Marchese, 1983).

3. Analytical procedure

Representative samples were selected for systematic electron microprobe (EMP) analysis. Wavelength-dispersive spectrometry (WDS) and energy-dispersive spectrometry (EDS) were performed at the Institut fuer Mineralogie und Kristallchemie, Universitaet Stuttgart, Germany, with a Cameca SX100 EMP with five spectrometers (analyser crystals: LLIF, 2 TAP, PET, LPET). 'Virtual WDS' (Reed and Buckley, 1998) software was applied to avoid interferences in background determinations. Natural and synthetic standards used were: K-feldspar (Si, Al, K), rhodonite (Mn), Fe_2O_3 (Fe), barite (Ba, La), rutile (Ti), albite (Na), Cr_3O_2 (Cr), diopside (Ca, Si, Mg), calcite (Ca), fluorite (F), $EuPO_4$ (Eu), $CePO_4$ (Ce), NaCl (Cl), Th-glass (Th), selenite (Sr), apatite (P, Ca) and U-glass (U). A voltage of 15 kV was combined with a constant beam current ranging from 7 to 10 nA, a take-off angle of 40°, and a variable spot beam diameter from 2 (for silicates) to 15μ (for carbonates). Manual, point by point, and automatic measurements were carried out.

Activation Laboratories Ltd., Ontario, Canada performed Sm/Nd isotope analyses on selected samples, which were milled and dissolved in a mixture of HF, HNO_3 and $HClO_4$. Before decomposition, the sample was spiked with a mixed $^{149}Sm/^{146}Sm$ solution. Rare-Earth elements (REEs) in the solution were separated using conventional cation-exchange techniques. Sm and Nd were then separated by extraction chromatography on HDEHP-covered Teflon powder. Analyses were performed on a Triton multi-collector mass-spectrometer (MC-MS). The accuracy of Sm and Nd content

measurements is ±0.5% (2σ) and that of the $^{147}Sm/^{144}Nd$ ratio ± 0.5% (2σ). $^{143}Nd/^{144}Nd$ ratios were determined relative to the value of 0.511860 for the La Jolla standard. Rb and Sr were also separated using conventional cation-exchange techniques and analysed with a Triton MC-MS in static mode. During the period of work the weighted average of 15 SRM-987 Sr-standard runs yielded 0.710238 ± 18 (2σ) for the $^{87}Sr/^{86}Sr$ ratio.

Additional isotope analysis of carbon from calcite was also performed by Activation Laboratories Ltd., Ontario, Canada, on a Finnigan MAT Delta Gas Isotope Ratio Mass Spectrometer, with a measurement precision of approximately 0.2‰. In K/Ar dating, the ^{40}K concentration was determined by Inductively Coupled Plasma (ICP) and the ^{40}Ar analysis using the isotope dilution procedure on a noble gas mass spectrometer.

Bulk chemical analyses of rocks were carried out by fusion ICP-MS. CO_2 was determined by coulometry, FeO by titration and H_2O^+ by gravimetry at Activation Laboratories Ltd., Ontario, Canada.

4. Petrography

4.1. SAV lamprophyre wall rock

A homogeneous, medium-to-coarse grained, grey coloured granite forms most of the Sierra Alta de Vela. Presumably, this rock corresponds to the so-called "old granitoids" (~2.1 Ga) and is composed of quartz, perthitic K-feldspar (microcline), some plagioclase (oligoclase) and scarce biotite laths. Zircon is an accessory phase. Retrogression of feldspars and biotite led to the formation of sericite and chlorite. Dynamic deformation of the granite is widespread but of different intensity, locally producing narrow belts of fine-grained red coloured ultramylonites as in the case of the wall rock at the studied UML in the southeastern tip of the Sierra Alta de Vela (Fig. 1, Fig. 2a). Although dynamic deformation affected the boundaries of the UML (Fig. 2b), this event does not reflect the high intensity of the wall rock deformation. The ultramylonite wall rock shows randomly distributed idiomorphic prismatic epidote at the contact (1–2 cm), indicating static growth and post-kinematic crystallization induced by the SAV UML intrusion heating or by associated late hydrous fluids. In addition, close to the contact, discordant veinlets derived from the altered SAV UML are present. They are formed by acicular amphibole (tremolite) and chlorite, cross-cutting the mylonitic foliation of the wall rock (Fig. 2a) and thus indicating post-kinematic metasomatism.

4.2. SAV lamprophyre dyke

The UML dyke is more than 40 m long and ~1 m thick, including incorporated wall-rock fragments (Fig. 2c). The dyke splits into branches parallel to the wall-rock foliation (dip direction/dip: 288°–310°/80°). The selvages of the dyke are well-foliated and massive in the centre. In addition, three different zones can be distinguished in the SAV UML dyke based on petrographic and mineralogic criteria:

(1) *Central zone*: this zone is characterized by a porphyric texture with Cr-rich clinopyroxene phenocrysts (Fig. 2d) and an almost panidiomorphic groundmass (Fig.3a), dominated by microphenocrysts of Cr-poor diopside. Additionally, variable and subordinate amounts of phlogopite and albite are present as primary minerals. Scarce aegirine-augite reaction rims (Fig. 3a), as well as calcite and garnet are mainly restricted to interstitial or ocellar texture areas (Fig. 3b). Zoned phlogopites are present as oiko-crysts including clinopyroxene associated with calcite or as veinlets. Opaque minerals and apatite are accessories.
(2) *Intermediate zone*: this zone is discontinuous. It is characterized by clinopyroxenes (as relictic patches of the central zone)

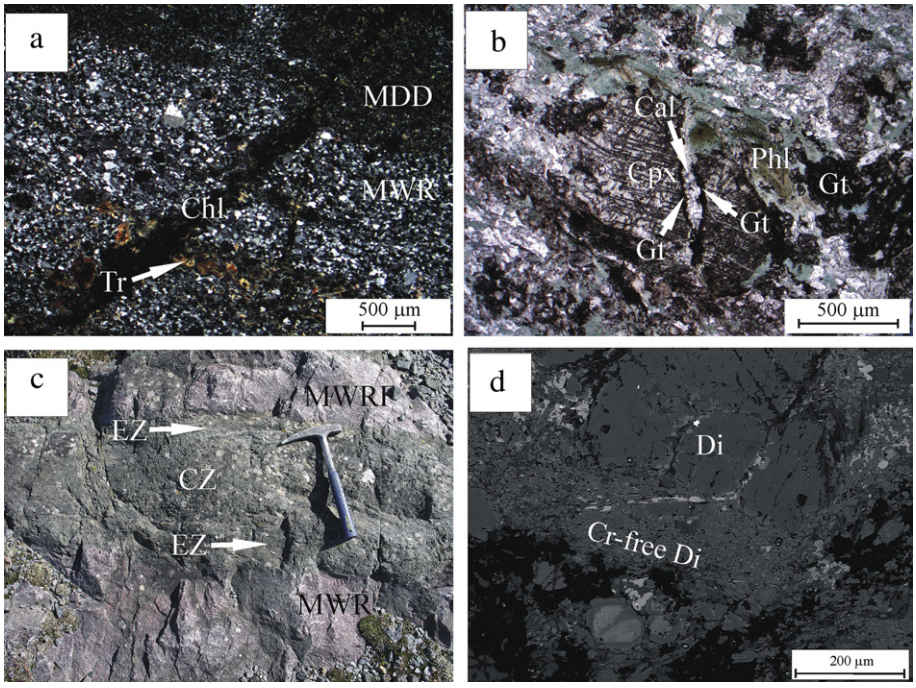

Fig. 2. (a) Mylonitic wall rock (MWR) derived from the "old granitoids", showing post-kinematic veinlets connected with the SAV UML (contact at upper right corner, MDD), formed by acicular tremolite (Tr) and chlorite (Chl). (b) Deformed clinopyroxene (Cpx) porphyroclast in an oriented matrix with the mineral assemblage of phlogopite and iron-rich phlogopite (Phl), andradite garnet (Gt) and calcite (Cal). Metasomatised external zone of the SAV UML. (c) Plan view of a branch of the SAV UML including a large mylonite wall rock fragment (MWRF). Note the oriented structure of the dyke branch at the contacts, forming the "external zone" (EZ), contrasting with the massive non-preferentially oriented "central zone" (CZ). (d) SEM backscattered images exhibiting a large phenocryst of Cr-rich diopside (Di), partially corroded, cross-cut by a flux of Cr-free microphenocrysts groundmass.

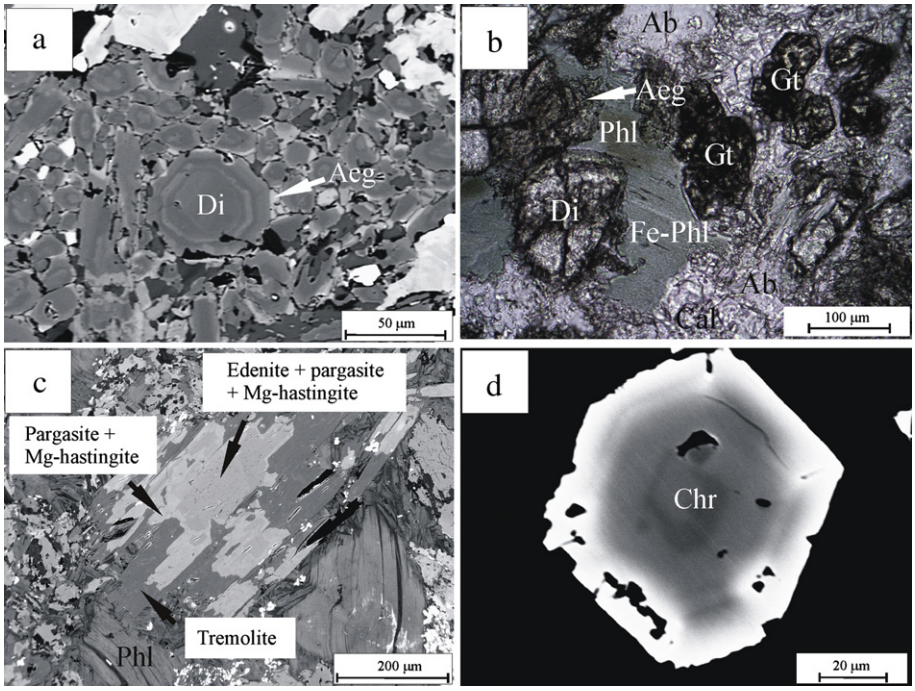

Fig. 3. (a) Backscattered SEM magnification image of a sector of the groundmass showing idiomorphic and strongly zoned Cr-free microphenocrysts of diopside (Di), with aegirine-augite rich rims (Aeg). (b). Ocellar texture in the central zone of the SAV UML, showing zoned oiko-crysts of phlogopite (Phl), iron-rich phlogopite (Fe-Phl), aegirine-augite rims (Aeg) growth on diopside (Di), idimorphic andradite garnet (Gt), albite (Ab) and calcite (Cal). Polarizer only. (c) Backscattered SEM image of strongly zoned crystal of amphibole surrounded by phlogopite (Phl). (d) Backscattered SEM image showing an idiomorphic (isometric hexoctahedral) strongly zoned crystal of chromite (Chr).

surrounded by considerable amounts of amphibole. The latter mineral is strongly zoned from core to rim (Fig. 3c). The mineral assemblage of this zone is composed of zoned phlogopite, garnet aggregates, sericite, calcite, titanite, albite, apatite and epidote.

(3) *External zone*: this zone shows a mineral assemblage characterized by oriented phyllosilicates (phlogopite, chlorite and sericite) and a groundmass of abundant aggregates of garnet, albite, calcite and apatite. Clinopyroxene is present as isolated, relictic, deformed and corroded porphyroclasts (Fig. 2b). Secondary quartz, titanite, epidote and mica-chlorite interstratifications have also been detected as alteration minerals.

5. Mineral chemistry

5.1. Clinopyroxene

Phenocrysts (>400 μm) in the lamprophyre are Cr-rich diopside, the rims of which reach up to 1.3 wt. % of Cr_2O_3, Table 1a. These phenocrysts are normally corroded, weakly deformed and show no marked zoning (Fig. 2d). The most significant cation substitutions of both diopside types (SiO_2/TiO_2 vs. MgO/FeO, SiO_2 vs. $Al_2O_3 + Cr_2O_3$, MgO vs. FeO, and TiO_2 vs. Al_2O_3) are presented in divariant diagrams in Fig. 4. Cr-free diopside microphenocrysts (15–50 μm, Fig. 4a, c) display a more widespread cation substitution of Fe–Mg, but with poorer MgO content than phenocrysts of Cr-rich diopside, which are richer in MgO. These microphenocrysts are a later generation which show strong oscillatory zoning, with almost no deformation. They are present in some samples of the central zone (Figs. 3a and 4a–d, and Table 1a and b). A weak enrichment in FeO and Fe_2O_3 (diopside to salite) from the core to the rims was determined in both diopside types, Fig. 4e. Cr-free and Cr-rich diopside types exhibit relatively extended SiO_2 vs. Al_2O_3 and SiO_2 vs. $Al_2O_3 + Cr_2O_3$ substitutions, respectively (Fig. 4b), the Cr-rich diopside type being relatively richer in SiO_2. An aegirine enrichment towards the rims of both diopsidic pyroxenes in the central zones of the dyke is frequently present (Fig. 4f).

5.2. Phlogopite

The primary phlogopite content in the central zone is about 10–20 vol.%. A clear zoning from Si–Mg-rich cores (pleochroism: X′ = colorless/Z′ = brown) towards the Fe–Al-rich rims (pleochroism: X′ = colorless/Z′ = green, Table 2, anal. 0116, 1 and 14) was determined in all the samples from the three study zones of the SAV UML. The phlogopite composition of the rims is described as "iron-rich phlogopite" from here on. Fig. 5a and Table 2 show a trend from phlogopite to eastonite–siderophyllite composition, typical for an UML, according to Rock (1991). Fig. 5b displays a positive correlation between BaO and TiO_2 with increasing content from core to rims. Guo and Green (1990) have proposed a plot with combined coupled substitutions to explain the complex compositional trends in phlogopites. In Fig. 5c the plot of samples from the SAV UML indicates that they fit well with mantle compositions, with the constraints of other individual substitution mechanisms introduced by Righter et al. (2002). The alteration of phlogopite generated intermediate phyllosilicate phases up to chlorite formation.

5.3. Chromite

This early formed and scarce mineral is frequently corroded. A systematic analysis using EMP was only possible with a few preserved idiomorphic crystals (Fig. 3d). The TiO_2 contents vary from 0.23 to 0.80 wt. %, showing a negative correlation with respect to Cr_2O_3 and a positive correlation with respect to Fe_2O_3 (Fig. 6a and b). A positive correlation between MnO (0.7–3.73 wt. %) and ZnO (0.04–2.86 wt. %) was also determined. Crystal cores are rich in Mg and Cr, whereas rims are rich in Al, Zn, Fe^{2+}, Mn, Ti and Fe^{3+},

Table 1a
EMP chemical analyses of pyroxenes from the SAV UML central zone. Including Cr-free diopside, Cr-rich diopside and aegirine–augite compositions.

Cr-rich diopside	SA-02 40	SA-02 39	SA-02 38	0216 30	0216 29	0116 38	0116 37	0116 36	0116 35	0116 34	0116 28	Cr-free diopside	SA-02 1	SA-02 2	SA-02 3	SA-02 6	SA-02 7	SA-02 8	SA-02 9	SA-02 20	SA-02 21
SiO_2	52.50	50.72	50.53	50.04	50.92	52.18	52.21	51.32	52.41	51.60	50.82	SiO_2	50.66	52.35	51.72	48.90	51.84	49.82	49.33	51.84	48.81
TiO_2	0.36	0.67	0.67	0.73	0.53	0.30	0.34	0.43	0.32	0.33	0.54	TiO_2	0.55	0.41	0.47	0.82	0.49	0.64	0.76	0.31	0.77
Al_2O_3	2.07	3.89	4.33	4.00	3.21	2.37	2.16	2.99	2.26	3.06	3.41	Al_2O_3	3.36	2.26	2.23	5.48	2.99	4.15	4.96	1.53	4.52
Fe_2O_3	0.00	0.00	0.00	0.00	0.00	0.00	0.00	0.00	0.00	0.00	0.00	Fe_2O_3	0.00	0.00	0.00	0.00	0.00	0.00	0.00	0.00	0.00
Cr_2O_3	0.49	0.30	0.73	0.57	1.14	1.11	0.69	0.91	0.68	1.34	1.16	Cr_2O_3	0.06	0.01	0.05	0.00	0.03	0.01	0.00	0.00	0.00
FeO	4.03	4.89	4.63	4.83	4.26	3.41	3.80	3.81	3.59	3.62	4.23	FeO	5.34	5.08	5.05	7.27	4.84	6.24	6.90	3.96	6.53
MnO	0.01	0.08	0.06	0.02	0.02	0.07	0.13	0.04	0.08	0.03	0.09	MnO	0.14	0.10	0.05	0.14	0.04	0.08	0.13	0.09	0.13
MgO	15.88	14.59	14.51	14.93	15.17	16.06	16.05	15.60	15.96	15.67	15.10	MgO	14.85	15.29	15.38	13.19	15.20	13.77	13.48	15.48	13.03
CaO	24.70	24.25	23.88	24.05	24.08	24.34	24.27	24.38	24.07	23.93	24.34	CaO	24.10	23.91	24.06	23.43	24.20	23.72	23.39	25.04	24.48
Na_2O	0.47	0.56	0.59	0.57	0.64	0.50	0.50	0.48	0.53	0.64	0.53	Na_2O	0.55	0.42	0.47	0.75	0.50	0.62	0.63	0.38	0.67
K_2O	0.00	0.02	0.01	0.01	0.02	0.00	0.02	0.00	0.00	0.02	0.00	K_2O	0.00	0.00	0.00	0.00	0.01	0.01	0.00	0.01	0.00
Total	100.51	99.97	99.94	99.75	99.99	100.34	100.17	99.96	99.90	100.24	100.22	Total	99.61	99.83	99.48	99.98	100.13	99.06	99.58	98.64	98.94
TSi	1.909	1.861	1.854	1.837	1.864	1.898	1.903	1.876	1.914	1.880	1.858	TSi	1.864	1.922	1.905	1.805	1.895	1.851	1.827	1.921	1.821
TAl	0.089	0.139	0.146	0.163	0.136	0.102	0.093	0.124	0.086	0.120	0.142	TAl	0.136	0.078	0.095	0.195	0.105	0.149	0.173	0.067	0.179
TFe^3	0.003	0.000	0.000	0.000	0.000	0.001	0.005	0.000	0.000	0.000	0.000	TFe^3	0.000	0.000	0.000	0.000	0.000	0.000	0.000	0.000	0.000
M_1Al	0.000	0.029	0.041	0.010	0.003	0.000	0.000	0.005	0.011	0.012	0.005	M_1Al	0.010	0.020	0.001	0.043	0.024	0.033	0.043	0.000	0.019
M_1Ti	0.010	0.018	0.018	0.020	0.015	0.008	0.009	0.012	0.009	0.009	0.015	M_1Ti	0.015	0.011	0.013	0.023	0.013	0.018	0.021	0.009	0.022
M_1Fe^3	0.000	0.000	0.000	0.000	0.000	0.000	0.000	0.000	0.000	0.000	0.000	M_1Fe^3	0.000	0.000	0.000	0.000	0.000	0.000	0.000	0.000	0.000
M_1Fe^2	0.115	0.146	0.125	0.136	0.122	0.089	0.099	0.107	0.091	0.092	0.123	M_1Fe^2	0.158	0.130	0.140	0.209	0.015	0.186	0.191	0.123	0.204
M_1Cr	0.014	0.009	0.021	0.017	0.033	0.032	0.020	0.026	0.020	0.039	0.033	M_1Cr	0.002	0.002	0.001	0.000	0.001	0.000	0.000	0.000	0.000
M_1Mg	0.861	0.798	0.794	0.817	0.828	0.871	0.872	0.850	0.869	0.849	0.823	M_1Mg	0.815	0.837	0.844	0.726	0.828	0.763	0.744	0.855	0.725
M_2Fe^2	0.007	0.004	0.017	0.012	0.008	0.015	0.017	0.010	0.018	0.019	0.006	M_2Fe^2	0.006	0.026	0.016	0.016	0.015	0.008	0.023	0.000	0.000
M_2Mn	0.000	0.002	0.002	0.001	0.001	0.002	0.004	0.001	0.002	0.001	0.003	M_2Mn	0.004	0.003	0.002	0.004	0.001	0.003	0.004	0.003	0.004
M_2Ca	0.962	0.953	0.939	0.946	0.945	0.949	0.948	0.955	0.942	0.934	0.954	M_2Ca	0.950	0.941	0.949	0.926	0.984	0.944	0.928	0.994	0.978
M_2Na	0.033	0.040	0.042	0.041	0.045	0.035	0.035	0.034	0.038	0.045	0.038	M_2Na	0.039	0.030	0.034	0.054	0.035	0.045	0.045	0.027	0.048
M_2K	0.000	0.001	0.000	0.000	0.001	0.000	0.001	0.000	0.000	0.001	0.000	M_2K	0.000	0.000	0.000	0.000	0.000	0.000	0.000	0.000	0.000
Sum cat.	4.000	3.999	4.000	4.000	3.999	4.000	3.999	4.000	4.000	3.999	4.000	Sum cat.	4.000	4.000	4.000	4.000	4.000	4.000	4.000	4.000	4.000
Wo	49.451	50.072	50.031	49.476	49.620	49.269	48.862	49.663	48.981	49.313	49.956	Wo	49.143	48.569	48.664	49.256	49.228	49.610	49.103	50.341	51.203
En	44.236	41.917	42.298	42.736	43.495	45.232	44.960	44.215	45.189	44.815	43.121	En	42.132	43.215	43.283	38.582	43.022	40.071	39.375	43.302	37.921
Fs	6.313	8.012	7.671	7.788	6.885	5.500	6.178	6.122	5.831	5.872	6.923	Fs	8.735	8.215	8.053	12.162	7.749	10.319	11.522	6.457	10.876

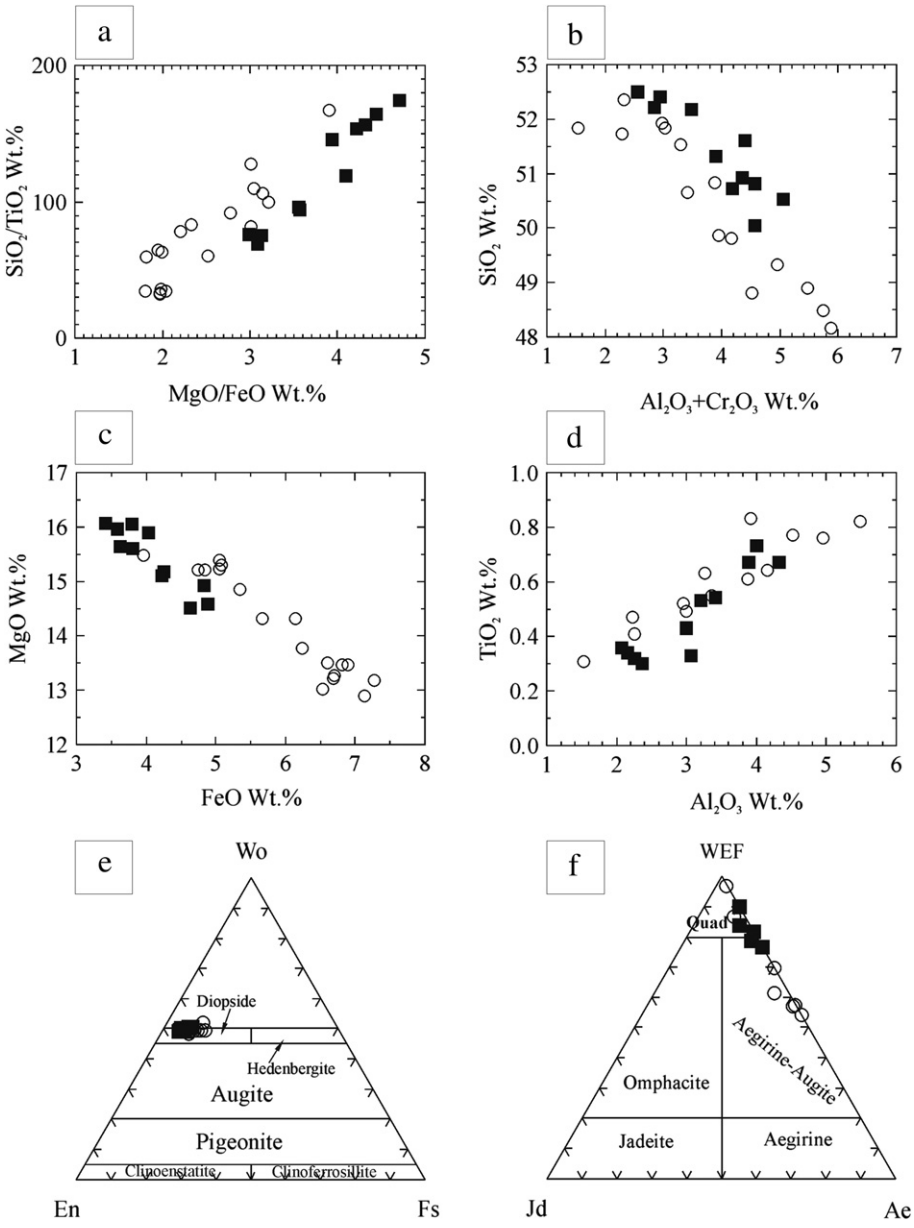

Fig. 4. (a) SiO_2/TiO_2 vs. MgO/FeO plot. (b) SiO_2 vs. $Al_2O_3 + Cr_2O_3$ plot. (c) MgO vs. FeO plot. (d) TiO_2 vs. Al_2O_3 plot. (e) En-Wo-Fs mole % plot. (f) Jd-WEF-Ae mole % plot. Empty circles represent Cr-free diopside crystals and filled squares represent Cr-rich diopside crystals.

indicating a progressively oxidizing environment at decreasing temperatures. Most of the analysed chromites lay at the base of Mitchell's (1986) "trend I" of spinel compositions in lamprophyres (graphic not shown), which is supposedly typical for kimberlites. Bornite and chalcopyrite are detected in minor amounts as other opaque accessory minerals in the central zone.

5.4. Amphibole

In the intermediate zone, the SAV UML developed an intense and compositionally variable amphibolitization involving the replacement of preexistent diopside and phlogopite. Amphibole crystallized, developing strong zoning, Fig. 3c. The core composition of amphiboles plots between edenite, pargasite and Mg-hastingite. A small intermediate rim with a composition close to pargasite + Mg-hastingite (Table 3) follows outwards. Finally, the external rim corresponds to an Al-poor tremolite, with incomplete Al saturation at tetrahedral positions (Table 3). The enrichment in amphibole minerals indicates that the magmas retained or acquired enough water during a late crystallization stage at crustal levels.

5.5. Garnet

The composition diagram for the andradite garnet reflects a relatively wide variation in Al and Fe(t) substitutions in the three studied zones of the SAV lamprophyre. Strong variations in Fe^{3+} – Al from core to rim in single crystals and vice versa can be observed, indicating crystallization under disequilibrium. An extremely rich Fe(t) composition, made up exclusively of Fe^{3+}, (Fig. 7) characterizes the more metasomatised external zone of the SAV lamprophyre. This zoned mineral is often finely intergrown with calcite and replaces preexistent minerals like clinopyroxene, amphibole and phlogopite. Garnet veinlets cross-cutting Cr-rich diopside may

Table 1b
EMP chemical analyses and structural formula of pyroxenes from the SAV UML central zone. Including Cr-free diopside, Cr-rich diopside and aegirine–augite compositions.

Cr-free diopside	SA-02 14	SA-02 15	SA-02 16	SA-02 17	SA-02 18	SA-02 19	SA-02 20	SA-02 21	SA-02 Pir-27	Aegirine–augite	SA-02 10	SA-02 11	SA-02 12	SA-02 23	SA-02 24	SA-02 27	SA-02 Pir-1	SA-02 Pir-2	SA-02 Pir-3	SA-02 Pir-9	SA-02 Pir-10
SiO_2	51.93	51.53	49.87	47.96	48.49	47.96	47.80	48.17	50.83	SiO_2	52.02	52.48	52.58	51.53	53.08	51.97	51.28	51.28	52.14	51.73	51.79
TiO_2	0.52	0.63	0.83	1.40	1.36	1.47	1.46	1.40	0.61	TiO_2	0.35	0.78	0.61	0.68	0.37	0.54	0.75	0.45	0.39	0.40	0.56
Al_2O_3	2.95	3.26	3.92	5.94	5.74	5.80	5.98	5.86	3.87	Al_2O_3	1.02	1.05	0.62	3.00	0.67	0.79	1.91	0.85	1.11	0.72	3.02
Fe_2O_3	0.00	0.00	0.00	0.00	0.00	0.00	0.00	0.00	0.00	Fe_2O_3	0.00	0.00	0.00	0.00	0.00	0.00	0.00	0.00	0.00	0.00	0.00
Cr_2O_3	0.03	0.03	0.03	0.04	0.01	0.05	0.05	0.02	0.02	Cr_2O_3	0.00	0.01	0.06	0.02	0.06	0.02	0.00	0.02	0.00	0.03	0.03
FeO	4.74	5.05	5.67	7.13	6.70	6.82	5.98	6.61	6.14	FeO	17.23	19.45	18.36	8.51	17.20	21.11	11.76	16.42	16.66	17.33	9.12
MnO	0.07	0.11	0.06	0.11	0.10	0.14	0.10	0.09	0.11	MnO	0.50	0.33	0.31	0.11	0.16	0.48	0.24	0.45	0.36	0.39	0.18
MgO	15.21	15.23	14.31	12.89	13.28	13.47	13.22	13.50	14.31	MgO	7.96	7.48	7.37	12.72	7.92	5.05	10.67	8.06	7.93	7.41	12.98
CaO	24.50	24.07	23.81	23.30	23.43	23.68	23.37	23.57	23.84	CaO	16.96	11.80	13.91	20.55	13.99	13.22	21.78	19.63	18.81	18.77	19.54
Na_2O	0.41	0.48	0.57	0.71	0.62	0.64	0.60	0.68	0.72	Na_2O	4.16	5.43	5.83	1.89	5.93	6.29	1.58	2.45	2.96	3.18	2.25
K_2O	0.00	0.00	0.00	0.02	0.01	0.01	0.02	0.00	0.09	K_2O	0.03	0.00	0.01	0.07	0.00	0.03	0.00	0.00	0.00	0.02	0.01
Total	100.36	100.39	99.07	99.52	99.74	100.04	99.29	99.90	100.54	Total	100.23	98.81	99.66	99.08	99.38	99.50	99.97	99.61	100.36	99.98	99.47
TSi	1.896	1.881	1.849	1.782	1.795	1.769	1.777	1.777	1.857	TSi	1.955	1.996	1.972	1.917	1.984	1.974	1.927	1.962	1.973	1.969	1.914
TAl	0.104	0.119	0.151	0.218	0.205	0.231	0.223	0.223	0.143	TAl	0.045	0.004	0.027	0.083	0.016	0.026	0.073	0.038	0.027	0.031	0.086
TFe^3	0.000	0.000	0.000	0.000	0.000	0.000	0.000	0.000	0.000	TFe^3	0.000	0.000	0.000	0.000	0.000	0.000	0.000	0.000	0.00	0.000	0.000
M_1Al	0.023	0.021	0.020	0.042	0.045	0.021	0.039	0.031	0.024	M_1Al	0.000	0.043	0.000	0.048	0.014	0.009	0.012	0.000	0.023	0.002	0.046
M_1Ti	0.014	0.017	0.023	0.039	0.038	0.041	0.041	0.039	0.017	M_1Ti	0.010	0.022	0.017	0.019	0.010	0.015	0.021	0.013	0.011	0.011	0.016
M_1Fe^3	0.000	0.000	0.000	0.000	0.000	0.000	0.000	0.000	0.000	M_1Fe^3	0.330	0.317	0.416	0.136	0.409	0.450	0.134	0.193	0.199	0.241	0.170
M_1Fe^2	0.134	0.133	0.165	0.204	0.184	0.197	0.186	0.187	0.179	M_1Fe^2	0.212	0.194	0.153	0.091	0.123	0.221	0.236	0.333	0.320	0.311	0.053
M_1Cr	0.001	0.001	0.001	0.001	0.000	0.001	0.001	0.001	0.001	M_1Cr	0.000	0.000	0.002	0.001	0.002	0.001	0.000	0.001	0.000	0.001	0.001
M_1Mg	0.828	0.829	0.791	0.714	0.733	0.741	0.733	0.742	0.779	M_1Mg	0.446	0.424	0.412	0.705	0.441	0.286	0.598	0.460	0.447	0.421	0.715
M_2Fe^2	0.010	0.021	0.011	0.017	0.023	0.014	0.022	0.017	0.008	M_2Fe^2	0.000	0.108	0.007	0.038	0.005	0.000	0.000	0.000	0.009	0.000	0.059
M_2Mn	0.002	0.003	0.002	0.003	0.003	0.004	0.003	0.003	0.003	M_2Mn	0.016	0.011	0.010	0.003	0.005	0.015	0.008	0.015	0.012	0.013	0.006
M_2Ca	0.958	0.941	0.946	0.927	0.929	0.936	0.931	0.932	0.933	M_2Ca	0.683	0.481	0.559	0.819	0.560	0.538	0.877	0.805	0.763	0.766	0.774
M_2Na	0.029	0.034	0.041	0.051	0.044	0.046	0.043	0.049	0.051	M_2Na	0.303	0.400	0.424	0.136	0.430	0.463	0.115	0.182	0.212	0.235	0.161
M_2K	0.000	0.000	0.000	0.001	0.000	0.000	0.001	0.000	0.004	M_2K	0.001	0.000	0.000	0.003	0.000	0.001	0.000	0.000	0.000	0.001	0.000
Sum cat.	4.000	4.000	4.000	3.999	4.000	4.000	3.999	4.000	3.996	Sum cat.	3.999	4.000	4.000	3.997	4.000	3.999	4.000	4.000	4.000	3.999	4.000
Wo	49.557	48.834	49.405	49.694	49.623	49.482	49.655	49.533	49.023	WEF	69.113	60.321	57.354	85.871	56.903	53.362	88.183	81.595	78.109	76.276	83.283
En	42.824	42.993	41.314	38.251	39.134	39.163	39.082	39.475	40.943	Jd	0.004	4.730	0.000	3.704	1.388	0.946	0.949	0.028	2.246	0.151	3.538
Fs	7.599	8.174	9.282	12.055	11.243	11.355	11.263	10.992	10.034	Ae	30.883	34.949	42.646	10.425	41.709	45.692	10.868	18.377	19.645	23.573	13.179

Table 2
EMP chemical analyses and structural formula of zoned phlogopites from the SAV UML. Analyses of sample 0116 (1 and 14) correspond to the so called "iron-rich phlogopite" in the text.

Sample	0116	0116	0116	0116	0116	0116	0116	0116	0116	0216	0216	0216	0216	0216	SA-02	SA-02	SA-02	SA-02	SA-02	SA-02	SA-02
Oxide	1	13	14	18	19	20	21	31	34	1	2	3	4	5	18	19	20	23	24	28	37
SiO_2	35.79	35.84	35.77	38.16	37.16	37.22	38.30	38.20	35.80	38.90	39.05	38.95	39.23	38.57	37.30	37.72	37.71	37.00	37.76	38.02	39.20
TiO_2	1.05	1.49	1.11	0.19	1.64	1.52	0.12	0.20	1.53	0.21	0.18	0.18	0.11	0.28	1.16	1.29	0.90	1.46	1.40	0.81	0.17
Al_2O_3	15.90	16.53	16.46	16.38	15.49	15.31	14.35	15.25	14.95	13.92	14.04	13.97	13.67	14.14	15.07	15.16	15.27	15.44	15.49	14.01	12.91
FeO	14.18	12.76	13.19	12.00	11.40	11.79	11.23	11.34	12.78	10.05	9.71	8.75	9.84	10.23	12.07	11.79	11.96	11.28	10.11	11.88	11.47
MnO	0.16	0.15	0.22	0.20	0.15	0.20	0.14	0.15	0.09	0.15	0.18	0.16	0.19	0.16	0.16	0.23	0.21	0.14	0.10	0.16	0.14
MgO	15.95	16.41	16.74	17.23	18.28	17.70	20.58	19.56	17.05	20.72	20.74	21.37	21.12	20.54	19.80	18.90	18.47	18.88	20.01	19.87	21.31
CaO	0.05	0.02	0.08	0.08	0.07	0.13	0.00	0.02	0.57	0.00	0.00	0.02	0.00	0.01	0.07	0.04	0.03	0.03	0.04	0.66	0.09
Na_2O	0.02	0.03	0.04	0.04	0.09	0.07	0.02	0.04	0.05	0.05	0.00	0.05	0.06	0.07	0.10	0.06	0.02	0.08	0.12	0.04	0.03
K_2O	9.65	9.92	9.90	10.18	9.01	9.72	9.38	10.01	10.02	10.39	10.83	10.60	10.21	10.35	8.80	9.85	10.27	9.83	9.24	8.79	8.22
BaO	0.91	1.11	0.91	0.02	1.21	1.03	0.00	0.04	0.77	0.08	0.16	0.09	0.00	0.11	0.63	0.67	0.57	0.99	0.82	0.47	0.23
F^-	0.74	0.76	0.80	1.03	0.88	0.79	1.36	1.28	0.90	2.07	1.39	1.79	1.72	1.71	0.74	0.78	0.80	0.78	0.87	0.75	1.19
Cl^-	0.00	0.02	0.00	0.00	0.00	0.01	0.00	0.00	0.00	0.00	0.00	0.01	0.00	0.00	0.01	0.02	0.00	0.00	0.00	0.00	0.00
H_2O	3.56	3.60	3.58	3.55	3.60	3.63	3.40	3.45	3.49	3.08	3.41	3.22	3.25	3.24	3.70	3.69	3.67	3.66	3.67	3.69	3.48
Total	97.96	98.64	98.80	99.06	98.98	99.12	98.88	99.54	98.00	99.62	99.69	99.16	99.41	99.41	99.61	100.20	99.88	99.57	99.63	99.15	98.44
Tot. corr.	97.65	98.32	98.46	98.62	98.61	98.79	98.31	99.00	97.62	98.75	99.11	98.41	98.69	98.69	99.30	99.86	99.54	99.24	99.26	98.84	97.94
Si	2.741	2.715	2.708	2.835	2.772	2.785	2.840	2.821	2.737	2.873	2.875	2.873	2.891	2.855	2.757	2.783	2.795	2.751	2.773	2.810	2.904
Al (T)	1.259	1.285	1.292	1.165	1.228	1.215	1.160	1.179	1.263	1.127	1.125	1.127	1.109	1.145	1.243	1.217	2.795	1.249	1.227	1.190	1.096
	4.000	4.000	4.000	4.000	4.000	4.000	4.000	4.000	4.000	4.000	4.000	4.000	4.000	4.000	4.000	4.000	4.000	4.000	4.000	4.000	4.000
Ti	0.061	0.085	0.063	0.010	0.092	0.086	0.006	0.011	0.088	0.011	0.010	0.010	0.006	0.015	0.065	0.072	0.050	0.082	0.077	0.045	0.009
Al (O)	0.176	0.190	0.177	0.269	0.134	0.135	0.094	0.149	0.084	0.085	0.093	0.087	0.079	0.089	0.070	0.101	0.129	0.103	0.114	0.044	0.031
Fe^{2+}	0.908	0.808	0.835	0.746	0.711	0.738	0.697	0.700	0.817	0.621	0.598	0.540	0.606	0.633	0.746	0.727	0.741	0.701	0.621	0.737	0.711
Mn	0.011	0.009	0.014	0.013	0.009	0.012	0.008	0.010	0.006	0.009	0.011	0.010	0.012	0.010	0.010	0.014	0.013	0.009	0.006	0.010	0.009
Mg	1.821	1.852	1.889	1.908	2.032	1.974	2.275	2.154	1.944	2.282	2.276	2.349	2.320	2.267	2.182	2.079	2.041	2.093	2.191	2.196	2.354
Sum	2.977	2.944	2.978	2.946	2.978	2.945	3.080	3.024	2.939	3.008	2.988	2.996	3.023	3.014	3.073	2.993	2.974	2.988	3.009	3.032	3.114
Ca	0.004	0.002	0.007	0.006	0.006	0.010	0.000	0.002	0.046	0.000	0.000	0.001	0.000	0.001	0.005	0.003	0.002	0.002	0.003	0.052	0.007
Na	0.004	0.005	0.006	0.005	0.014	0.011	0.003	0.006	0.007	0.007	0.000	0.008	0.008	0.010	0.014	0.009	0.003	0.012	0.017	0.006	0.005
K	0.943	0.959	0.956	0.964	0.858	0.928	0.887	0.943	0.977	0.979	1.017	0.997	0.960	0.977	0.830	0.927	0.971	0.932	0.866	0.831	0.777
Ba	0.027	0.033	0.027	0.005	0.035	0.030	0.000	0.001	0.023	0.002	0.004	0.002	0.000	0.003	0.018	0.019	0.017	0.029	0.024	0.014	0.007
Sum	0.978	0.999	0.996	0.980	0.913	0.979	0.890	0.952	1.053	0.988	1.021	1.008	0.968	0.990	0.867	0.958	0.993	0.975	0.910	0.903	0.796
F	0.180	0.181	0.191	0.241	0.208	0.186	0.318	0.299	0.218	0.482	0.323	0.416	0.401	0.400	0.174	0.181	0.187	0.184	0.203	0.175	0.279
Cl	0.000	0.022	0.000	0.000	0.000	0.001	0.000	0.000	0.000	0.000	0.000	0.001	0.000	0.000	0.001	0.003	0.000	0.000	0.000	0.000	0.000
H	1.820	1.817	1.809	1.758	1.792	1.813	1.682	1.701	1.782	1.518	1.677	1.583	1.599	1.600	1.825	1.816	1.813	1.816	1.797	1.825	1.701

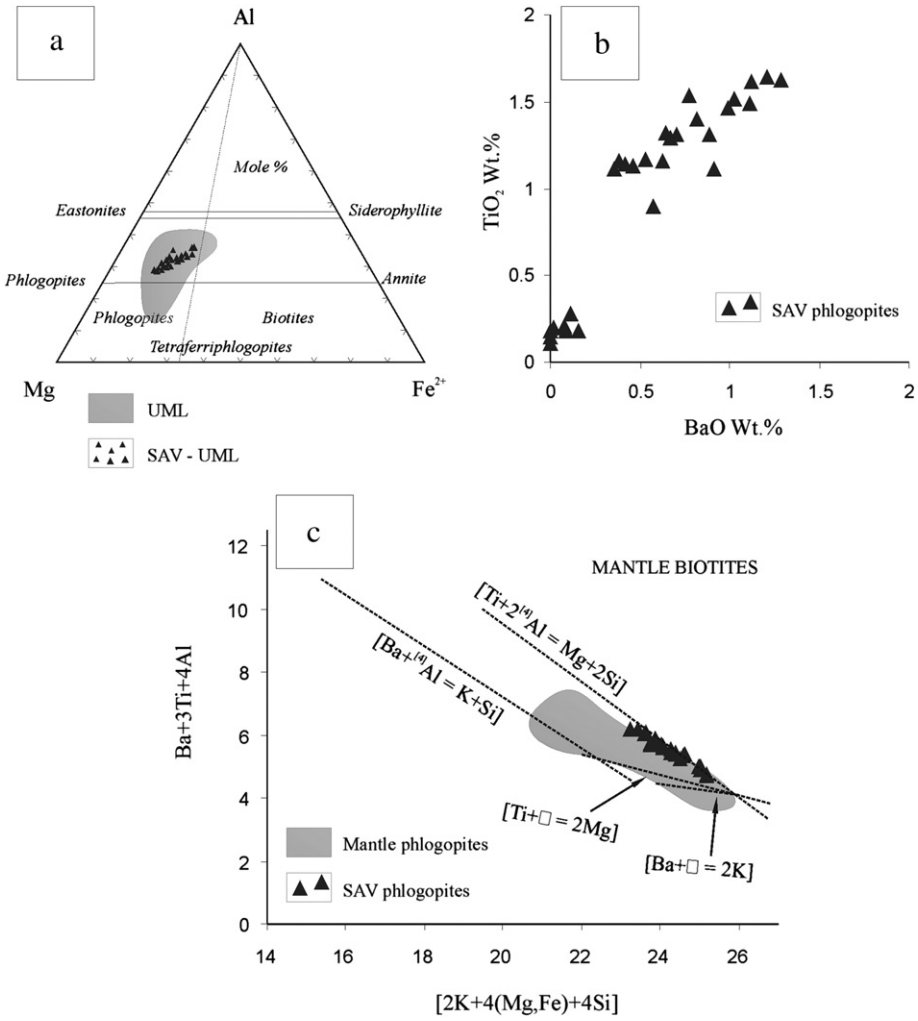

Fig. 5. (a) Mica compositions of the SAV UML plotted in the field of UML (Rock, 1991). (b) Plot BaO vs. MgO in phlogopites of the SAV UML. (c) Plot of compositional mantle phlogopites from different authors and individual substitutions mechanisms discussed by Righter et al. (2002).

have high chromium contents (Table 4, sample SA-02, 41, 42 and 43). The occasional occurrence of andradite garnet surrounding chromite crystals was observed, with Cr-enrichment in the garnet close to chromite.

5.6. Albite

This feldspar is unique to the SAV UML and reaches 10%–20% in vol., existing interstitially and as ocelli in the central zone. The crystallization of this primary end-member mineral clearly post-dates clinopyroxene and phlogopite. In the external zone it probably overlaps with the formation of tremolite associated with deformation, thus reducing the availability of Al and Na as reflected in the tremolite due to the breakdown of Mg-hastingsite to tremolite + albite at decreasing temperatures.

5.7. Calcite

This mineral is present in all the studied samples in the three described zones of the SAV UML, and in the wall rocks in contact with the dyke. It is considered a primary phase, which is later affected by crustal fluids (see carbon and oxygen isotopy section). The H_2O/CO_2 ratio clearly increases from the central to the external zone of the dyke, Table 5. Calcite frequently exhibits fine intergrowths with garnet (andradite) and is associated with albite, forming an ocellar texture (Fig. 3b). EMP analyses show that it is almost pure calcite with low MgO (0.03–1.29 wt. %), FeO (0.18–0.24 wt. %) and MnO (0.16–0.17 wt. %) contents.

5.8. Sericite

Sericite is a later mineral replacing pre-existing minerals such as phlogopite. It is frequently associated with iron-rich phlogopite and chlorite. This mineral assemblage is abundant in the external zone of the SAV UML which represents the most hydrated part of the lamprophyre as a consequence of K-metasomatism (up to almost 6 wt. % of H_2O^+ and 3.2 wt. % of K_2O (Table 5-sample 0116, Fig. 9). The intermediate zone is also affected by the presence of iron-rich phlogopite and sericite (4.0 wt. % of H_2O^+ and 2.65 wt. % of K_2O (Table 5-sample 0216).

6. Whole rock composition

The occurrence of several small dykes close to the studied UML is shown in Fig. 1. The chemical analyses of these dyke rocks (Table 5) were plotted in an AFM diagram (Fig. 8) and correspond mostly to the calc-alkaline series defined by Iacumin et al. (2001) and Teixeira et al. (2002) for other areas of the Tandilia belt. This

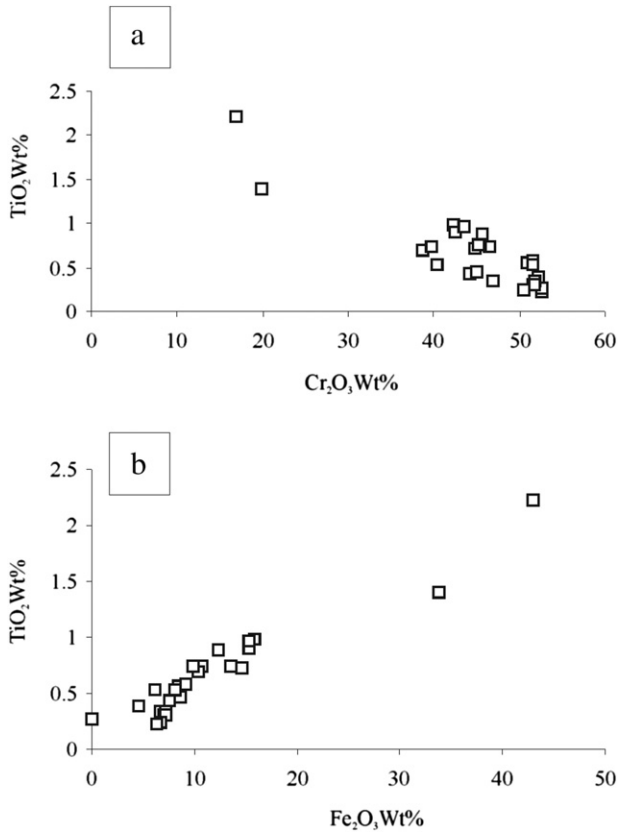

Fig. 6. (a) Plot TiO_2 vs. Cr_2O_3 showing negative correlation in chromites from the SAV UML. (b) Plot TiO_2 vs. Fe_2O_3 showing positive correlation in chromites from the SAV UML.

series has so far not been detected in the SAV. Only one of these dyke rocks, which is undeformed, plots on the trend of the tholeiitic series. Our data for the undeformed tholeiitic dyke (0816) corresponds to that defined by Iacumin et al. (2001) as belonging to the high TiO_2 group, with 2.00 wt. %, Table 5. The calc-alkaline dykes studied in the SAV are all deformed and correspond to: fine-grained basaltic dyke (0117), amphibolic andesite dyke (0817), rhyodacite dyke (0716) and monzogranitic dyke (0217), Table 5.

SAV UML dyke gave: SiO_2 (41.4–48.2 wt. %), Cr (980–610 ppm), Ni (130–300 ppm) and Mg # (76–80), Table 4 (100 × molar Mg/(Mg + ∑Fe*), calculating total Fe* = Fe as FeO (Rudnick, 1995).

The chemical analyses of the most pristine samples of the SAV lamprophyre (0317 and SA-02, Table 4) also exhibit marked variations in their SiO_2 content. Such variations can be explained to a large extent by the strong and randomly mineral ratio variation (in vol. %) involving the main rock-forming minerals clinopyroxene and phlogopite (SiO_2 49–52 vs. 35–38 wt. %, respectively) and the variable presence of primary albite (SiO_2 = 67 wt. %), an effect that can be attributed to the rapid and chaotic crystallization of this type of rocks.

Moreover, the average sum of alkaline oxides in the alkaline lamprophyres is around 5 wt. % whereas the UML gave a mean of 3 wt. %, according to Rock (1991). Our data from the more pristine SAV UML samples are very close to 3 wt. %, Table 5.

The elements Cr, Co and Ni have mean values of 97, 38 and 65 ppm in alkaline lamprophyres, contrasting clearly with average values of 480, 75 and 430 ppm corresponding to UML, (Rock 1991). The mean values of 705 (Cr), 41 (Co) and 145 (Ni) ppm for SAV lamprophyre are indicative of a more typical ultramafic character. The average Mg # is 67 for alkaline lamprophyres and 77 for ultramafic lamprophyres, (Rock, 1991). Our mean data showing Mg # 78 for the more pristine SAV rocks confirms the ultramafic signature of this rare lamprophyre.

Table 3
EMP chemical analyses and structural formula of zoned amphiboles from the SAV UML intermediate zone. Analyses 1–7 correspond to pargasite–edenite–Mg hastingite compositions. Analyses 16, 22 and 34 correspond to pargasite–Mg hastingite compositions. Numbers 17–23 correspond to tremolite compositions.

Sample	0216-3	0216-3	0216-3	0216-3	0216-3	0216-3	0216-3	0216-3	0216-3	0216-3	0216-3	0216-3	0216-3	0216-3	0216-3
Oxide	1	2	3	5	6	7	16	22	34	17	18	19	20	21	23
SiO_2	42.80	43.02	43.20	44.14	44.06	43.88	41.86	41.77	42.62	57.20	56.75	57.10	55.12	56.83	56.73
TiO_2	1.28	1.24	1.16	0.91	0.97	0.85	0.10	0.15	0.29	0.03	0.00	0.01	0.10	0.02	0.01
Al_2O_3	10.14	10.06	9.68	9.22	9.30	9.27	11.48	11.08	10.45	0.21	0.38	0.25	0.83	0.23	0.33
Cr_2O_3	0.00	0.01	0.01	0.02	0.01	0.00	0.16	0.04	0.56	0.08	0.05	0.07	0.16	0.10	0.04
Fe_2O_3	4.10	4.59	7.44	5.41	3.66	6.00	9.64	7.36	6.82	1.57	1.03	0.73	0.00	1.32	2.35
FeO	7.69	7.39	5.33	6.58	8.16	6.36	6.79	9.17	8.41	4.69	5.91	4.98	6.16	4,70	4.85
MnO	0.20	0.18	0.15	0.19	0.19	0.21	0.21	0.25	0.26	0.15	0.21	0.14	0.19	0.20	0.20
MgO	15.20	15.27	15.34	15.61	15.40	15.45	12.59	12.06	12.86	20.85	20.24	20.84	19.95	20.86	20.29
CaO	11.66	11.53	10.93	11.40	11.69	11.34	9.63	9.32	9.93	12.76	13.09	12.86	14.39	13.12	12.66
Na_2O	3.58	3.56	3.44	3.31	3.44	3.31	4.31	5.00	4.35	0.49	0.32	0.42	0.30	0.24	0.42
K_2O	0.77	0.85	0.74	0.75	0.79	0.74	0.63	0.60	0.63	0.06	0.09	0.12	0.15	0.04	0.06
F^-	0.56	0.57	0.47	0.46	0.51	0.66	0.49	0.45	0.37	0.23	0.14	0.36	0.17	0.20	0.29
Cl^-	0.01	0.01	0.05	0.02	0.00	0.01	0.00	0.01	0.01	0.00	0.00	0.00	0.00	0.00	0.00
H_2O	1.76	1.76	1.81	1.83	1.80	1.72	1.80	1.78	1.83	2.06	2.09	1.98	2.04	2.06	2.02
Total	99.75	100.04	99.75	99.84	100.09	99.80	99.66	99.10	99.37	100.39	100.29	99.85	99.57	99.92	100.26
Tot. corr.	99.51	99.79	99.54	99.64	99.87	99.52	99.46	98.91	99.21	100.30	100.24	99.70	99.49	99.83	100.13
Si	6.319	6.328	6.343	6.468	6.474	6.447	6.221	6.287	6.358	7.923	7.907	7.951	7.781	7.912	7.896
Al-T	1.681	1.672	1.657	1.532	1.526	1.553	1.779	1.713	1.642	0.034	0.062	0.041	0.139	0.038	0.054
Σ	8.000	8.000	8.000	8.000	8.000	8.000	8.000	8.000	8.000	7.957	7.969	7.992	7.920	7.950	7.950
Ti	0.142	0.137	0.128	0.101	0.107	0.094	0.011	0.017	0.032	0.003	0.000	0.001	0.011	0.002	0.001
Al-O	0.083	0.071	0.019	0.061	0.086	0.052	0.232	0.253	0.195	0.000	0.000	0.000	0.000	0.000	0.000
Cr	0.000	0.002	0.001	0.002	0.001	0.000	0.019	0.005	0.066	0.009	0.006	0.007	0.018	0.011	0.005
Fe^{3+}	0.455	0.509	0.822	0.596	0.405	0.663	1.078	0.833	0.766	0.164	0.108	0.076	0.000	0.138	0.246
Fe^{2+}	0.949	0.909	0.654	0.806	1.003	0.782	0.844	1.154	1.049	0.543	0.689	0.580	0.728	0.547	0.564
Mn	0.025	0.023	0.019	0.024	0.024	0.026	0.027	0.032	0.033	0.018	0.024	0.017	0.023	0.023	0.024
Mg	3.346	3.349	3.357	3.410	3.374	3.383	2.789	2.706	2.859	4.306	4.204	4.326	4.328	4.328	4.210
Σ	5.000	5.000	5.000	5.000	5.000	5.000	5.000	5.000	5.000	5.043	5.031	5.007	5.108	5.049	5.050

(*continued on next page*)

Table 3 (*continued*)

Sample	0216-3	0216-3	0216-3	0216-3	0216-3	0216-3	0216-3	0216-3	0216-3	0216-3	0216-3	0216-3	0216-3	0216-3	0216-3
Oxide	1	2	3	5	6	7	16	22	34	17	18	19	20	21	23
Ca	1.844	1.817	1.720	1.789	1.840	1.785	1.533	1.502	1.587	1.894	1.953	1.919	2.176	1.956	1.888
Na	1.025	1.014	0.980	0.940	0.979	0.942	1.243	1.460	1.257	0.133	0.089	0.112	0.081	0.065	0.113
K	0.145	0.160	0.138	0.140	0.149	0.138	0.118	0.114	0.119	0.011	0.015	0.021	0.026	0.007	0.010
Σ	3.014	2.991	2.838	2.869	2.968	2.865	2.894	3.076	2.963	2.038	2.057	2.052	2.283	2.028	2.011
F	0.262	0.267	0.219	0.211	0.237	0.307	0.218	0.212	0.174	0.099	0.060	0.158	0.077	0.089	0.127
Cl	0.002	0.032	0.011	0.004	0.000	0.003	0.000	0.002	0.001	0.000	0.001	0.001	0.001	0.000	0.000
H	1.735	1.730	1.771	1.785	1.762	1.690	1.782	1.786	1.825	1.901	1.939	1.841	1.922	1.911	1.873

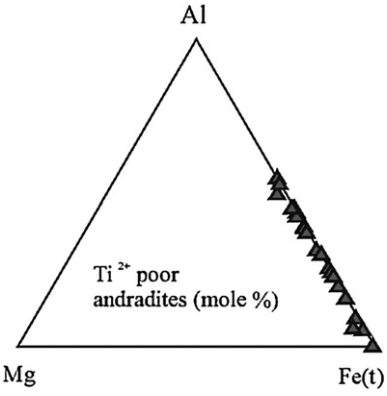

Fig. 7. Plot of Mg–Al–Fe(t) in Ti–Zr-poor andradite (mole %) from Rock (1991). Note the extended Al–Fe(t) substitutions in samples from the three zones of the SAV UML.

Fig. 8 shows that the most pristine samples of the central zone (samples 0317 and SA-02 in Table 5) of the SAV UML are the least evolved of the calc-alkaline series and may represent the precursor magma of the series.

6.1. Mass transfer

Metasomatic changes were revealed by petrographic observation between the most pristine samples of the central zone and those deformed and replaced from the external zone. Gresens' method (1967) modified by Grant (1986) of balancing volume (or mass) and element concentrations was applied in order to quantify the changes using the programme Geoiso Window™ developed by Coelho (2005). The altered rock (0116, 2.90 g/cm^3) plotted against the original concentration (0317, 3.05 g/cm^3), defines the isocon, i.e., a straight line through the origin. As shown in Fig. 9, we used the oxides TiO_2–Al_2O_3 and the element vanadium as less mobile and geochemically dissimilar components, which plot reasonably well on the isocon of constant mass during the alteration. Most of the major and trace elements are in the field of losses. In the gains field, H_2O, K_2O and Rb represent the abundance of iron-rich phlogopite, enabling Al_2O_3, FeO, H_2O^+ and TiO_2 to be fixed in the altered external zone. The two former oxides are also retained by the formation of andradite garnet. P_2O_5 in the gains field represents the increase in apatite in the altered sample. The breakdown of pyroxenes is reflected by the loss of Na_2O, CaO, MgO, SiO_2 and Sr and Ba. The loss of SiO_2 can be explained by the abundance of iron-rich

Table 4
EMP chemical analyses and structural formula of zoned garnets from the SAV UML central zone (samples 0316-1, 0316-2) and external zone (sample 0116-1). Analyses of sample SA-02 (41,42 and 43) correspond to a garnet veinlet cross-cutting a Cr-rich diopside crystal.

Sample	0316-1	0316-1	0316-1	0316-1	0316-1	0316-1	0316-1	0316-2	0316-2	0316-2	0116-1	0116-1	SA-02	SA-02	SA-02
Oxide	core 1	int. 2	int. 3	rim 4	core 5	int. 6	rim 7	core 8	int. 9	rim 10	core15	rim16	41	42	43
SiO_2	35.71	35.42	36.27	37.05	35.85	35.91	37.24	35.89	35.49	35.21	35.31	36.53	35.83	35.71	35.94
TiO_2	0.82	2.64	1.30	0.45	1.47	2.10	0.05	2.28	2.44	0.04	0.00	2.05	0.75	1.56	1.56
Al_2O_3	5.30	7.67	9.04	11.79	7.85	8.35	11.94	9.03	7.57	1.18	0.19	10.57	2.68	3.22	1.60
Cr_2O_3	0.01	0.01	0.02	0.01	0.00	0.02	0.00	0.03	0.03	0.02	0.00	0.06	0.48	1.90	1.03
Fe_2O_3	23.35	17.81	17.87	15.14	19.22	17.20	15.22	16.64	18.57	29.43	31.07	14.10	26.53	22.59	27.49
MgO	0.03	0.04	0.03	0.05	0.04	0.04	0.02	0.02	0.03	0.02	0.01	0.03	0.02	0.16	0.29
MnO	0.18	0.21	0.33	0.45	0.32	0.29	0.49	0.38	0.24	0.13	0.21	0.30	0.15	0.23	0.22
FeO	0.00	0.32	0.00	0.00	0.00	0.04	0.00	0.21	0.00	0.00	0.00	0.28	0.00	0.59	0.42
CaO	32.14	34.41	34.42	34.84	34.50	34.63	34.74	34.60	34.48	33.18	33.24	35.02	33.83	33.52	33.01
Na_2O	0.03	0.01	0.02	0.03	0.03	0.01	0.01	0.00	0.06	0.00	0.02	0.01	0.02	0.00	0.01
K2O	0.02	0.01	0.01	0.01	0.01	0.01	0.00	0.02	0.02	0.00	0.01	0.00	0.00	0.05	0.00
Total	99.58	98.57	99.29	99.82	99.29	98.60	99.71	99.10	98.93	99.20	100.06	98.95	100.30	99.59	100.56
Si	2.945	2.913	2.943	2.948	2.926	2.939	2.965	2.918	2.910	2.981	2.981	2.945	2.975	2.974	2.992
Al-T	0.055	0.087	0.057	0.052	0.074	0.061	0.035	0.082	0.090	0.019	0.019	0.055	0.025	0.026	0.008
Sum	3.000	3.000	3.000	3.000	3.000	3.000	3.000	3.000	3.000	3.000	3.000	3.000	3.000	3.000	3.000
Al-O	0.461	0.657	0.807	1.054	0.681	0.744	1.085	0.783	0.642	0.099	0.000	0.949	0.237	0.290	0.149
Cr	0.001	0.001	0.001	0.001	0.000	0.001	0.000	0.002	0.002	0.001	0.000	0.004	0.032	0.125	0.068
Fe^{3+}	1.449	1.103	1.091	0.906	1.180	1.059	0.912	1.018	1.146	1.875	1.974	0.855	1.658	1.415	1.722
Ti	0.051	0.164	0.079	0.027	0.090	0.129	0.003	0.139	0.151	0.002	0.000	0.124	0.047	0.097	0.035
Sum	1.962	1.924	1.978	1.988	1.951	1.933	2.000	1.942	1.941	1.977	1.974	1.930	1.974	1.927	1.974
Fe^{2+}	0.000	0.022	0.000	0.000	0.000	0.003	0.000	0.014	0.000	0.000	0.000	0.019	0.000	0.041	0.029
Mg	0.003	0.005	0.003	0.006	0.004	0.005	0.003	0.002	0.004	0.003	0.001	0.003	0.002	0.019	0.036
Ca	3.017	3.033	2.992	2.971	3.017	3.036	2.964	3.014	3.030	3.010	3.006	3.024	3.010	2.991	2.944
Mn	0.013	0.015	0.022	0.030	0.022	0.020	0.033	0.026	0.017	0.009	0.015	0.021	0.011	0.017	0.015
Na	0.004	0.001	0.003	0.005	0.005	0.002	0.001	0.000	0.009	0.000	0.004	0.001	0.003	0.000	0.001
Sum	3.037	3.076	3.020	3.012	3.048	3.066	3.001	3.056	3.060	3.022	3.026	3.068	3.026	3.073	3.026

Table 5
Rock chemical analyses carried out by ICP-MS of the SAV UML and associated dykes suite. Major oxides in wt. %, traces in ppm. UML: ultra-mafic lamprophyre, Bas. dy: basic dyke, Rhyod: rhyodacite dyke, Andes: Andesite dyke, T. Bas: Tholeiitic basalt dyke, Gra. dy: Granitic dyke.

Sample	0116	0216	0316	0317	SA-02	0117	0716	0817	0816	0217		0116	0216	0316	0317	SA-02	0117	0716	0817	0816	0217
Oxide	UML	UML	UML	UML	UML	Bas. dy	Rhyod	Andes	T. bas.	Gra. dy		UML	UML	UML	UML	UML	Bas. dy	Rhyod	Andes	T. Bas.	Gra. dy
SiO_2	41.40	44.21	44.40	48.22	44.77	45.81	67.95	56.09	46.78	64.85	Ti	4077	3297	4017	2398	3657	8033	2338	5396	11,990	3297
TiO_2	0.68	0.55	0.67	0.40	0.61	1.34	0.39	0.90	2.00	0.55	Y	41.00	26.90	21.10	489.00	12.40	37.40	21.30	17.40	33.90	17.10
Al_2O_3	12.82	9.87	9.35	7.22	9.30	16.67	14.03	16.87	14.56	16.01	Th	2.16	5.21	4.11	1.47	3.02	1.07	12.10	4.46	1.73	8.76
Fe_2O_3	2.52	4.00	4.29	2.73	8.74	13.44	4.53	8.87	15.05	0.78	U	0.36	1.18	0.74	0.32	0.85	3.71	2.66	0.91	0.38	2.03
FeO	7.44	5.15	4.86	3.56	–	–	–	–	–	4.00	Cr	770	980	950	800	610	180	40	50	100	60
MnO	0.16	0.18	0.17	0.13	0.15	0.17	0.08	0.17	0.21	0.10	Ni	230	300	230	130	160	100	<20	<20	80	<20
MgO	17.27	15.81	15.66	13.69	13.89	10.23	1.07	3.66	5.88	1.59	Co	65	59	55	38	44	55	10	34	58	13
CaO	4.79	10.09	11.73	15.97	13.56	1.92	3.36	7.35	9.16	4.30	Sc	241	29	41	71	39	31	9	22	32	12
Na_2O	1.31	1.74	1.32	1.71	1.97	2.88	3.14	3.05	2.62	3.45	V	243	162	187	143	187	118	25	107	146	50
K_2O	3.21	2.65	2.25	1.51	1.15	0.60	2.61	1.49	0.75	2.33	Cu	70	170	<10	<10	170	<10	20	20	40	10
P_2O_5	0.42	0.13	0.12	0.12	0.20	0.55	0.12	0.20	0.93	0.12	Pb	<5	<5	<5	<5	<5	<5	18	6	6	18
CO_2	0.92	1.15	1.18	1.69	2.35	–	–	–	–	–	Zn	90	80	80	50	70	150	70	110	160	70
H_2O^+	5.84	4.02	4.14	2.05	3.08	–	–	–	–	1.19	Sb	1	<0.5	0.70	0.90	<0.5	0.90	0.70	<0.5	0.70	<0.5
LOI	–	–	–	–	–	5.88	1.18	2.01	1.89	–	P	1832	567	523	523	872	2399	523	872	4056	523
Total	98.78	99.552	100.14	99.00	99.77	99.49	98.46	100.86	100.76	99.27	La	41.70	43.40	35.70	24.80	48.20	8.73	41.90	24.20	35.70	40.90
H_2O/CO_2	6.34	3.49	3.51	1.04	1.31	–	–	–	–	–	Ce	79.80	92.00	71.80	51.60	81.00	23.90	84.20	51.40	80.50	84.30
Mg #	76	76	76	80	76	60	32	45	43	38	Pr	9.32	11	8.88	6.64	9.74	3.36	9.19	5.85	10.10	8.91
K	26,646	21,998	18,667	12,535	9546	4981	21,666	12,368	6226	19,341	Nd	32.80	39.30	32.70	26.2	34.10	14.80	32.30	23.00	41.20	33.80
Ba	323	452	327	1773	390	120	934	831	1369	754	Sm	4.19	5.63	4.90	4.20	5.15	3.90	5.21	4.29	7.50	5.83
Rb	158	112	70	71	73	28	89	67	33	87	Eu	1.16	1.37	1.28	1.13	1.36	0.76	1.09	1.18	2.14	1.33
Sr	241	393	208	931	1362	46	298	435	422	388	Gd	2.85	3.35	3.21	2.99	3.52	4.29	3.71	3.53	6.31	4.51
Cs	16.8	5.80	41.00	4.60	6.30	0.50	1.60	1.90	1.10	1	Tb	0.32	0.47	0.39	0.38	0.46	0.80	0.52	0.52	0.92	0.60
Ga	13	11	11	7	9	30	20	21	20	21	Dy	1.56	2.44	2.01	1.87	2.38	4.94	2.86	2.96	5.18	3.24
Tl	0.64	0.43	0.27	0.28	0.30	0.12	0.35	0.22	0.18	0.45	Ho	0.29	0.46	0.40	0.35	0.46	1.05	0.57	0.59	1.05	0.62
Ta	0.13	0.48	0.37	0.10	0.20	0.42	0.56	0.32	0.68	0.57	Er	0.80	1.31	1.15	1.10	1.27	3.30	1.66	1.74	3.11	1.77
Nb	4.30	14.50	12.00	3.60	5.20	8.3	6.90	6.10	12.90	8.30	Tm	0.11	0.20	0.18	0.19	0.18	0.53	0.26	0.27	0.45	0.25
Hf	0.60	1.00	1.10	1.00	1.10	2.40	4.50	2.90	3.70	6.50	Yb	0.69	1.23	1.05	1.14	1.14	3.44	1.69	1.76	2.83	1.70
Zr	22	41	40	32	36	115	179	133	173	310	Lu	0.10	0.17	0.15	0.15	0.17	0.50	0.25	0.26	0.43	0.28

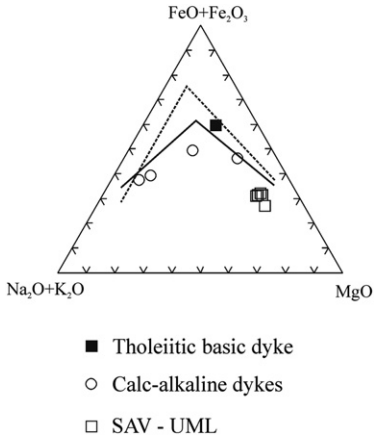

Fig. 8. AFM diagram for SAV dyke suite. Calc-alkaline-tholeiitic boundary (solid curve) as proposed by Irvine and Baragar (1971); tholeiitic trend (dashed curve) after Macdonald and Katsura (1964). Symbols: empty square, UML; empty circles, calc-alkaline series and filled square, tholeiitic basalt.

phlogopite and andradite, minerals of relatively low SiO_2 content, replacing original pyroxenes. Most HREE and HFSE are roughly aligned in the field of losses, whereas LREE are mostly aligned along the isocon. As a consequence of the processes of deformation and later metasomatism, a volume loss of ~38% could be calculated in the external zone of the SAV UML with respect to the central zone.

6.2. REE and multi-element diagrams

Chondrite-normalized REE patterns for the SAV UML samples show a shallow negative slope from LREE to HREE with an enrichment in LREE (Fig. 10a). The diagram exhibits a relatively consistent pattern with little variation between pristine samples of SAV UML. There is no Eu anomaly, indicating that plagioclase alone was not fractionated in parental magmas. The diagram of the metasomatized sample 0116 from the external zone of the SAV UML (not plotted in Fig. 10a), shows HREE loss, as registered in the isocon diagram (Fig. 9).

The calc-alkaline dykes of Teixeira et al. (2002), I rock, with $La/Lu_N = 13$ and an average of D4 rocks of Iacumin et al. (2001), with $(La/Lu)_N = 21–26$, were plotted together with the most pristine SAV UML samples $(La/Lu)_N = 17–29$ in Fig. 10a. The LREE pattern in the two groups is quite similar. The HREE content in the SAV UML samples is relatively lower than that of the calc-alkaline dykes. This behaviour can be attributed to the extremely low content in Zr (an average of 34 ppm taking all five samples in the SAV UML Table 5). The low content in Zr also confirms the mafic signature of the studied rock. The negative Eu anomaly in the D_4 rocks of Iacumin et al. (2001) can be imputed to fractionation of plagioclase in the parental magma.

Multi-element diagrams of more pristine samples of the SAV UML normalized to chondrite show Nb–Ta, P (strong) and Ti (small) negative anomalies, suggesting that the magma generating this rock may have previously experienced an incompatible element enrichment of the mantle source (Fig. 10b), probably by underthrust of the oceanic crust (Massonne, 2004; Stern, 2008; Massonne et al., 2012). The strong positive Y anomaly in one sample is typical of alkaline and ultramafic lamprophyres ($Y > 150$ ppm, Rock, 1991).

Multi-elemental plots of calculated (batch melting; Hanson, 1978) mantle source normalized to PM (Primitive Mantle) for the calc-alkaline magma (D3, of Iacumin et al., 2001), related to the Tandilia belt Transamazonian Orogeny event, are characterized by negative Nb, P and Ti anomalies. This pattern is similar to that obtained for more pristine SAV UML samples normalized to the same PM (Sun and McDonough, 1989), Fig. 10c.

7. $^{87}Sr/^{86}Sr$ and $^{143}Nd/^{144}Nd$ isotopy

The isotope ratios were recalculated to the time of emplacement ($t = 1.93$ Ga), giving rise to the End (T) and initial $^{87}Sr/^{86}Sr$ bulk rock values represented in Table 6a. The ε_{Nd} values are all fairly negative, between −3.67 and −4.37, indicating an enriched mantle source (Fig. 11a). This fact agrees with the high values of the initial Sr ratios (~0.711). These isotopic ratios could be interpreted as the result of crustal contamination, but in view of the nature of this rock, we favour the enriched mantle source explanation. Based on geochemical and petrological inferences, Iacumin et al. (2001) and Teixeira et al. (2002) also concur with the absence of crustal

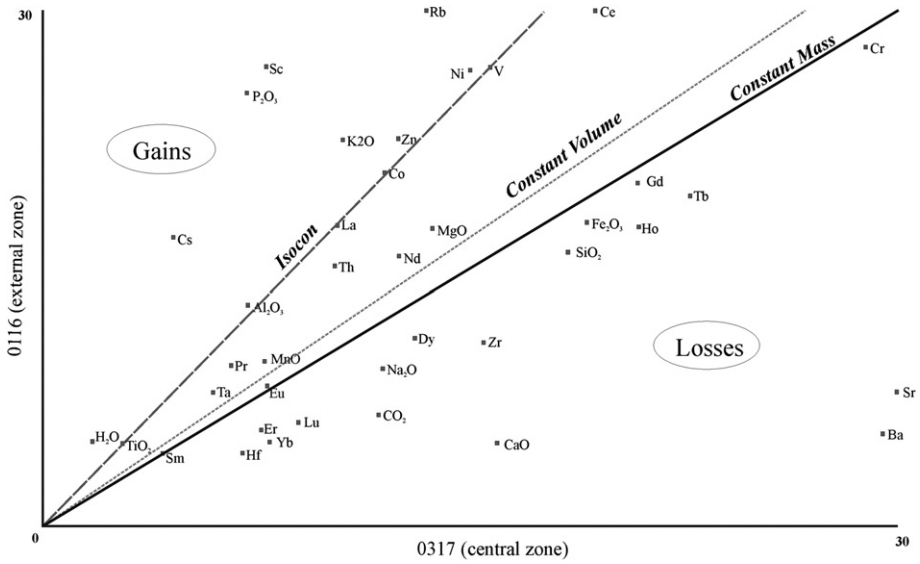

Fig. 9. Isocon diagram of an unaltered sample (0317) from central zone of the SAV UML against the deformed and metasomatized sample (0116), from the external zone of the SAV UML. Immobile elements for isocon are TiO_2–Al_2O_3–V.

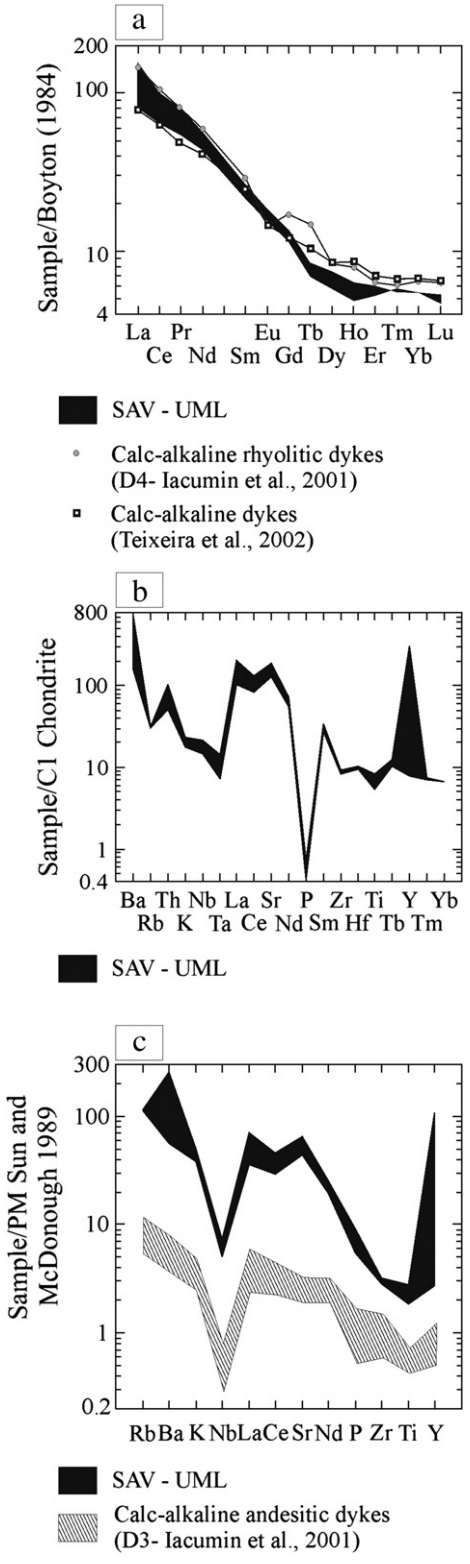

Fig. 10. (a) Chondrite normalized diagram of REE (after Boyton, 1984) for most pristine SAV UML samples and SAV calc-alkaline series; (b) C_1 chondrite normalized spider diagram for the most pristine samples of SAV UML. (c) Multielemental plot of the most pristine samples of the SAV UML and calculated mantle source for calc-alkaline (D3) primary magmas of the Tandilia belt (Iacumin et al., 2001). See text for more details.

Table 6a
Sr–Nd isotope composition of representative samples from the SAV UML.

Sample	Rb (ppm)	Sr (ppm)	$^{87}Sr/^{86}Sr_m$	$^{87}Sr/^{86}Sr_i$
03171109	71	931	0.72111	0.71492
SA-02	73	1362	0.71244	0.70809
01160410	158	241	0.76390	0.71071
02160410	112	393	0.71268	0.68956?

Sample	Sm (ppm)	Nd (ppm)	$^{143}Nd/^{144}Nd_i$	$(\varepsilon_{Nd})_i$	$T_{(DM)}$
03171109	6.54	40.29	0.51120	−3.67	2.42
SA-02	4.79	29.96	0.51118	−3.67	2.41
01160410	5.11	36.8	0.51099	−4.19	2.40
02160410	5.55	39.64	0.51109	−4.37	2.29

contamination in the calc-alkaline dyke swarms of the Tandilia belt. The data of D3 rocks group (calc-alkaline) of Iacumin et al. (2001) coincide fairly with those of SAV UML, as can be seen in Fig. 11a.

The T_{DM} values around 2.4 Ga (Table 6a) most probably indicate that the event of mantle enrichment took place just before the magma generation, assuming the enriched mantle model.

One initial Sr data (0.689558, Table 6a) is meaningless. This may have been caused by geochemical modifications due to metasomatism affecting sample 02160410 sometime after its emplacement.

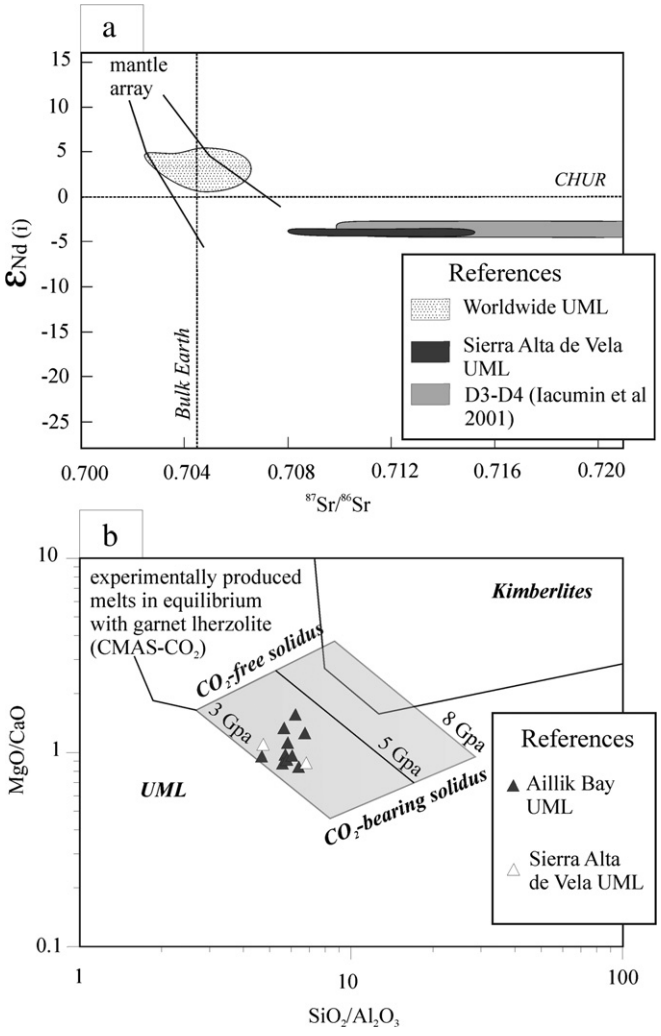

Fig. 11. (a) ε_{Nd} vs. $^{87}Sr/^{86}Sr$ for the SAV UML. Mantle array and worldwide UML occurrences (b) "UML–kimberlite discrimination diagram" from Rock (1991), modified by Tappe et al. (2006). Shaded fields of experimentally determined melt compositions after Gudfinnsson and Presnall (2005).

8. Carbon and oxygen isotopy

The samples selected for stable isotopic analyses correspond to the three described zones, including a vein cross-cutting the metasomatised lamprophyre (04160410, Table 6b). The $\delta^{13}C$ (PDB) ‰ data (−5.5 to −7.4, Table 6b) indicate a mean value similar to that of UML around the world. Post-magmatic processes have been shown to have little effect on the C isotopic composition, but may produce major changes in O isotopes (Deines, 1989; Santos and Clayton, 1995), processes that surely affected the SAV UML fluids generating the strong negative values (−17.1 to −20.1, Table 6b) of the $\delta^{18}O_{SMOW}$ in ‰.

9. K–Ar geochronology

The studied SAV UML, which intrudes the deformed granitic field rock, yielded a minimum K–Ar age of 1928 ± 54 Ma (Table 6c), determined on a single phlogopite hand-picked under the binocular microscope from one of the most pristine rocks of the central zone. This data fits well with the Transamazonian Orogeny (2.1–1.9 Ga). Moreover, the outcrop of calc-alkaline rocks only several metres away from the studied rock, with an equivalent age and emplacement orientation, strongly suggests that SAV UML belongs to the calc-alkaline series. Consequently, we assume that the granitic wall rock of the SAV UML corresponds to the "old granitoids" of the Tandilia belt of Early Proterozoic age (~2.1 Ga).

10. Discussion

The petrological and geochemical attributes of the SAV UML indicate a magma derived from an enriched mantle source, as also suggested Iacumin et al. (2001) for the associated calc-alkaline dyke swarms series of the Tandilia belt. According to these authors, both calc-alkaline and tholeiitic dykes occur in a very restricted area, particularly in Tandil, indicating important small-scale mantle heterogeneity. The outcrop of calc-alkaline rocks only several metres away from the studied rock, with an equivalent age and emplacement orientation, strongly suggest that SAV UML belongs to the calc-alkaline rock series.

The early crystallizing minerals in the precursor SAV UML magma, diopside and chromite, may have formed during pyroxene fractionation at relatively low pressures, where chromium was rejected from the diopside crystals of the mantle. We have measured Cr rich-diopside phenocrysts of up to 1.3 wt. % of Cr_2O_3, which represent relicts of mantle diopside in the SAV UML. The phlogopite composition exhibits similar mantle characteristics (Fig. 5c). The later formed Cr-free diopside microphenocrysts (Figs. 3a and 4a–d) and chromite (Fig.6a and b) displays intense zoning due to disequilibrium during rapid magma ascent and the corresponding temperature decrease. The same characteristics were observed for the minerals later crystallizing as amphiboles. A period of Na-rich residual magmatic fluids developed shortly after Cr-free diopside formation, involving the formation of aegirine-augite rims on both diopside types. The dominant and strongly zoned amphiboles (Fig. 7) with an Na-rich core in the intermediate zone of the SAV UML, are probably initially related to the same Na-rich residual fluids event and reflect conditions of lower pressure and temperature. This may have been induced by synkinematic events during the ascent to the emplacement at higher crustal levels. The ocellar texture and veinlets representing this stage of fluid-rich influx affected the central zone only weakly but the intermediate and external zones more intensively.

Table 6b
Carbon and oxygen isotope composition of calcite from SAV UML rocks

Sample	$\delta\ ^{13}C_{PDB}$ in ‰	$\delta^{18}O_{SMOW}$ in ‰
SA-02	−5.50	−17.7
01160410	−7.37	−18.2
02160410	−6.46	−18.5
03170409	−6.14	−19.5
04160410	−6.64	−20.1

Table 6c
K–Ar minimum age of phlogopite from the most pristine SAV UML rock.

Sample	% K	$^{40}Ar_{rad}$, nl/g	% $^{40}Ar_{air}$	Age, Ma
03171109 B	5.51	724.7	0.6	1928 ± 54

The transitional banded structure of the SAV UML lamprophyre is clearly related to the pristine main mineralogy (central zone) and metasomatic changes derived from a later injection of fluids preferentially in the intermediate and external zones. As Fig. 2b shows, the SAV UML dyke is strongly deformed close to the contact with the wall rock (dyke external zone), a phenomenon which probably occurred during the emplacement, generating a preferred orientation in the original minerals. A late metasomatic evolved fluid phase (K, P and water rich, Fig. 9) affected the deformed minerals forming the dominant chlorite, iron rich-phlogopite, andradite, apatite and sericite assemblage in the external zone. According to Iacumin et al. (2001) the emplacement of calc-alkaline dykes in the Tandilia belt is associated with the transtensional stage of the Transamazonian Orogeny, which is fully consistent with the minimum phlogopite crystallization age of the SAV UML. In the external zone of the SAV dyke, neither aegirine enrichment nor amphibole growth towards the pyroxene rims can be observed, due to the intense and later metasomatism (Fig. 2b) suffered by the pyroxenes and amphiboles. A progressively higher H_2O/CO_2 ratio from the central to external zone of the SAV UML can be observed (Table 5), which may respond to the increase in fluids contamination as corroborated by the values between −17.7 and −20.1 of $\delta^{18}O_{SMOW}$ in calcite, Table 6b.

Teixeira et al. (2002) established a 2020 ± 24 Ma $^{40}Ar/^{39}Ar$ biotite age (from two baked wall rocks) for the calc-alkaline dykes and 2150 Ma for the granitic country rocks. Our K–Ar minimum age of 1928 ± 54 Ma for the SAV UML can be considered close to that of 2020 Ma, if an age decrease during coetaneous tectonic and post-tectonic metasomatism took place. Varela et al., 1985 determined a Rb–Sr isochron (errorchrone?) giving an age of 1623 ± 100 Ma for the deformed granitic rocks located at the south of the SAV, where the SAV UML is emplaced. We suggest that the evident granitic deformation may have affected this data, since even a modest increase in temperature of 100–200 °C could have drastic effects on the parent–daughter isotopic relationships (Faure, 1977).

Plotting the most pristine samples from the SAV UML dyke on the MgO/CaO vs. SiO_2/Al_2O_3 "UML–kimberlite discrimination diagram" from Rock (1991), modified by Tappe et al. (2006) (Fig. 11b), shows that they are approximately aligned along the 3.5 GPa pressure line, within the areas of experimentally produced melts in equilibrium with garnet lherzolites. The most pristine samples of the SAV UML also plot within the aillikite–damtjernite original lamprophyric magma compositions of Tappe et al. (2006).

Iacumin et al. (2001) tested the crystal fractionation process by performing MELTS (Ghiorso and Sack, 1995) and XLFRAC (Stormer and Nicholls, 1978) methods on the Proterozoic basic suite swarms of the Tandilia belt, taking into account that plagioclase was not in a liquid phase at the earliest stages of the differentiation process, as effectively occurred in the SAV UML. The mantle source calculated by Iacumin et al. (2001) shows coincidences with the more pristine samples of the SAV UML (Fig. 10c).

11. Conclusions

The SAV UML may represent the original precursor magma for the calc-alkaline series, which, after a differentiation process in the form of fractional crystallization, generated the suite of calc-alkaline hypabyssal rocks of the study area.

Exceptionally deep tectonic events during the Transamazonian Orogeny would enable part of the magma to ascend rapidly for emplacement at upper crustal levels as undifferentiated magma.

The SAV UML wall rock granite should be assigned to "old granitoids" of the Tandilia belt of Early Proterozoic age ($\sim$2.1 Ga).

The SAV UML is the first well-documented presence of an UML in the Tandilia belt basement, part of the southernmost Rio de la Plata Craton.

Acknowledgements

We wish to thank the Alexander von Humboldt Stiftung (Projekt/V-FoKoop ARG/1005980) and ANPCYT (PICT 2006 N° 249) for financial support. Thomas Theye (Stuttgart) is also acknowledged for his support with the EMP work. Arne Willner and an anonymous reviewer are acknowledged for their recommendations which helped us improve on the earlier version of the manuscript.

References

Boyton, W.V., 1984. Geochemistry of the rare earth elements: meteorite studies. In: Rare Earth Element Geochemistry. Elsevier, pp. 63–114.

Coelho, J., 2005. GEOISO-A Windows™ program to calculate and plot mass balances and volume changes occurring in a wide variety of geologic processes. Computers and Geosciences 32, 1523–1528.

Cingolani, C.A., Santos, J.O.S., McNaughton, N.J., Hartmann, L.A., 2005. Geocronología U-Pb SHRIMP sobre circones del granito Montecristo, Tandil, provincia de Buenos Aires, Argentina. In: XVI Congreso Geológico Argentino, Actas, vol. 1, pp. 299–302 (Buenos Aires).

Dalla Salda, L., Iñiguez Rodríguez, A.M., 1979. La Tinta, Precámbrico y Paleozoico de Buenos Aires. In: VII Congreso Geológico Argentino, Actas, vol. 1, pp. 539–550 (Buenos Aires).

Dalla Salda, L.H., Francese, J., 1985. Los granitoides de Tandil. In: Segundas Jornadas Geológicas Bonaerenses, Actas. Comisión de Investigaciones Científicas de la provincia de Buenos Aires, La Plata, pp. 845–861.

Deines, P., 1989. Stable isotope variations in carbonatites. In: Bell, K. (Ed.), Carbonatites: Genesis and Evolution. Unwin Hyman, London, pp. 301–359.

Di Paola, E.C., Marchese, H.G., 1974. Relación entre tectosedimentación, litología y mineralogía de arcillas del Complejo Buenos Aires y la Formación La Tinta, (prov. de Buenos Aires). Revista de la Asociación Argentina de Mineralogía, Petrología y Sedimentología 5 (3–4), 45–58.

Dristas, J.A., 1983. Petrología de una metariolita de la Sierra del Tigre, Tandilia. Revista de la Asociación Geológica Argentina 38 (2), 235–247.

Faure, G., 1977. Principles of Isotope Geology. John Wiley and Sons, New York, p. 81.

Ghiorso, M.S., Sack, R.O., 1995. Chemical mass transfer in thermodynamic model for the interpolation and extrapolation of liquid-solid equilibria in magmatic system at elevated temperatures and pressures. Contributions to Mineralogy and Petrology 119, 197–212.

Grant, J.A., 1986. The isocon diagram: a simple solution to Gresens' equation for metasomatic alteration. Economic Geology 81, 1976–1982.

Gresens, R.L., 1967. Composition-volume relationships of metasomatism. Chemical Geology 2, 47–55.

Gudfinnsson, G.H., Presnall, D.C., 2005. Continuous gradations among primary carbonatitic, kimberlitic, melilititic, basaltic, picritic, and komatiitic melts in equilibrium with garnet lherzolite at 3–8 GPa. Journal of Petrology 46, 1645–1659.

Guo, J., Green, T.H., 1990. Experimental study of Ba partitioning between phlogopite and silicate liquid at upper mantle pressure and temperature. Lithos 24, 83–95.

Hanson, G.N., 1978. The application of trace elements to the petrogenesis of igneous rocks of granitic composition. Earth and Planetary Science Letters 38, 26–43.

Hartmann, L.A., Santos, J.O.S., Cingolani, C.A., McNaughton, N.J., 2002. Two Paleoproterozoic orogenies in the evolution of the Tandilia Belt, Buenos Aires, as evidenced by zircon U-Pb SHRIMP geochronology. International Geology Review 44, 528–543.

Iacumin, M., Piccirillo, E.M., Girardi, V.A.V., Teixeira, W., Bellieni, G., Echeveste, H., Fernández, R., Pinese, J.P.P., Ribot, A., 2001. Early Proterozoic calc-alkaline and Middle Proterozoic tholeiitic dyke swarms from central-eastern Argentina: petrology, geochemistry, Sr-Nd isotopes and tectonic implications. Journal of Petrology 42 (11), 2109–2143.

Iñiguez, A.M., Del Valle, A., Poiré, D., Spalletti, L.A., Zalba, P., 1989. Cuenca Precámbrica-Paleozoica Inferior de Tandilia, prov. de Buenos Aires. In: Cuencas sedimentarias argentinas. Serie Correlación Geológica, vol. 6. Instituto Superior de Correlación Geológica, Universidad Nacional de Tucumán, pp. 245–263. Asociación Geológica Argentina, Buenos Aires.

Irvine, T.N., Baragar, W.R.A., 1971. A guide to the chemical classification of the common volcanic rocks. Canadian Journal of Earth Sciences 8, 523–548.

Lema, H.A., Cucchi, R.J., 1981. Hallazgo de meta-vulcanitas en el cerro Tandileufú. Revista de la Asociación Geológica Argentina 36 (2), 103–104.

Lema, H.A., Cucchi, R.J., 1985. Geología de la Sierra Alta de Vela. In: Segundas Jornadas Geológicas Bonaerenses, Actas. Comisión de Investigaciones Científicas de la provincia de Buenos Aires, La Plata, pp. 867–879.

Leveratto, M.A., Marchese, H.G., 1983. Geología y estratigrafía de la Fm. La Tinta (y homólogas) en el área clave de Sierra de la Tinta-Barker-Villa Cacique-Arroyo Calaveras, provincia de Buenos Aires. Revista de la Asociación Geológica Argentina 38, 235–247.

Macdonald, G.A., Katsura, T., 1964. Chemical composition of Hawaiian lavas. Journal of Petrology 5, 82–133.

Massonne, H.-J., 2004. Ultra-high pressure metamorphism. In: Encyclopedia of Geology, vol. 5. Elsevier, pp. 533–540.

Massonne, H.-J., Dristas, J.A., Martínez, J.C., 2012. Metamorphic evolution of the Rio de la Plata Craton, in the Cinco Cerros area, Buenos Aires province, Argentina. Journal of South American Earth Sciences 38, 57–70.

Mitchell, R.H., 1986. Kimberlites: Mineralogy, Geochemistry and Petrology. Plenum Press, New York, p. 442.

Pankhurst, R.J., Ramos, A., Linares, E., 2003. Antiquity and evolution of the Río de la Plata craton in Tandilia, southern Buenos Aires province, Argentina. Journal of South American Earth Sciences 16, 5–13.

Quartino, B.J., Villar Fabre, J.F., 1967. Geología y petrología del basamento de Tandil y Barker (provincia de Buenos Aires) a la luz del estudio de las localidades críticas. Revista de la Asociación Geológica Argentina XXII (3), 223–251.

Rapela, C.W., Pankhurst, R.J., Casquet, C., Fanning, C., Baldo, E.G., González-Casado, J.M., Galindo, C., Dahlquist, J., 2007. The Río de la Plata craton and the assembly of SW Gondwana. Earth Science Reviews 83, 49–82.

Reed, S.J.B., Buckley, A., 1998. Rare-earth element determination in minerals by electron-probe micro-analysis: application of spectrum synthesis. Mineralogical Magazine 62, 1–8.

Righter, K., Dyar, M.D., Delaney, J.S., Vanemann, T.W., Hervig, R.L., King, P.L., 2002. Correlation of octahedral cations with OH^- O^{2-}, Cl^- and F^- in biotites from volcanic rocks and xenoliths. The American Mineralogist 87, 142–153.

Rock, N.M.S., 1991. Lamprophyres. Blackie and Son Ltd., London, p. 288.

Rudnick, R., 1995. Making continental crust. Nature 378, 571–578.

Santos, R.V., Clayton, R.N., 1995. Variations of oxygen and carbon isotopes in carbonatites: a study of Brazilian alkaline complexes. Geochimica et Cosmochimica Acta 59, 1339–1352.

Stern, R.J., 2008. Modern-style plate tectonics began in Neoproterozoic time: an alternative interpretation of the Earth's tectonic history. Geological Society of America, Special Paper 440, 265–280.

Stormer, J.C., Nicholls, J., 1978. XLFRAC: a program for interactive testing of magmatic differentiation models. Computers and Geosciences 4, 143–159.

Sun, S.S., McDonough, W.F., 1989. Chemical and Isotopic Systematics of Oceanic Basalts: Implications for Mantle Composition and Processes. In: Geological Society of London Special Publication, vol. 42, pp. 313–345.

Tappe, S., Foley, S.F., Jenner, G.A., Heaman, L.M., Kjargaard, B.A., Romer, R.L., Stracke, A., Joyce, N., Hoefs, J., 2006. Genesis of ultramafic lamprophyres and carbonatites at Aillik Bay, Labrador: a consequence of incipient lithospheric thinning beneath the North Atlantic craton. Journal of Petrology 47 (7), 1261–1315.

Teixeira, W., Pinese, J.P.P., Iacumin, M., Girardi, V.A.V., Piccirillo, E.M., Echeveste, H., Ribot, A., Fernandez, R., Renne, P.R., Heaman, L.M., 2002. Calc-alkaline and tholeiitic dyke swarms of Tandilia, Rio de la Plata craton, Argentina: U-/Pb, Sm-Nd, and Rb-Sr 40Ar/39Ar data provide new clues for intraplate rifting shortly after the Trans-Amazonian Orogeny. Precambrian Research 119, 329–353.

Varela, R., Dalla Salda, L., Cingolani, C., 1985. La edad Rb-Sr del granito de la Vela, Tandil. In: Primeras Jornadas Geológicas Bonaerenses, Actas. Comisión de Investigaciones Científicas de la provincia de Buenos Aires, La Plata, pp. 881–890.